The Astrophysical Journal, 934:160 (25pp), 2022 August 1 https://doi.org/10.3847/1538-4357/ac7a46

Galactic Winds across the Gas-rich Merger Sequence. II. Lyα Emission and Highly Ionized O VI and N V Outflows in Ultraluminous Infrared Galaxies

Weizhe Liu (刘伟哲)[1], Sylvain Veilleux[1,2], David S. N. Rupke[3], Todd M. Tripp[4], Frederick Hamann[5], and Crystal Martin[6]
[1] Department of Astronomy, University of Maryland, College Park, MD 20742, USA; oscarlwz@gmail.com
[2] Joint Space-Science Institute, University of Maryland, College Park, MD 20742, USA
[3] Department of Physics, Rhodes College, Memphis, TN 38112, USA
[4] Department of Astronomy, University of Massachusetts, Amherst, MA 01003, USA
[5] Department of Physics and Astronomy, University of California, Riverside, CA 92507, USA
[6] Department of Physics, University of California, Santa Barbara, CA, 93106, USA
Received 2022 April 22; revised 2022 June 10; accepted 2022 June 16; published 2022 August 3

Abstract

This paper is the second in a series aimed at examining the gaseous environments of $z \leqslant 0.3$ quasars and ultraluminous infrared galaxies (ULIRGs) as a function of AGN/host galaxy properties across the merger sequence. This second paper focuses on the Lyα emission and O VI 1032, 1038 and N V 1238, 1243 absorption features, tracers of highly ionized gas outflows, in ULIRGs observed with HST/COS. Lyα emission is detected in 15 out of 19 ULIRGs, and 12 of the 14 clear Lyα detections show emission with blueshifted velocity centroids and/or wings. The equivalent widths of the Lyα emission increase with increasing AGN luminosities and AGN bolometric fractions. The blueshifts of the Lyα emission correlate positively with those of the [O III] λ5007 emission, where the latter traces the ionized gas outflows. The Lyα escape fractions tend to be slightly larger in objects with stronger AGN and larger outflow velocities, but they do not correlate with nebular line reddening. Among the 12 ULIRGs with good continuum signal-to-noise ratios, O VI and/or N V absorption features are robustly detected in six of them, all of which are blueshifted, indicative of outflows. In the combined ULIRG + quasar sample, the outflows are more frequently detected in the X-ray weak or absorbed sources. The absorption equivalent widths, velocities, and velocity dispersions of the outflows are also higher in the X-ray weak sources. No other strong correlations are visible between the properties of the outflows and those of the AGN or host galaxies.

Unified Astronomy Thesaurus concepts: Galaxy evolution (594); Quasars (1319); Interstellar medium wind (848); AGN host galaxies (2017); Active galactic nuclei (16)

1. Introduction

Major mergers of gas-rich galaxies, both near and far, are a paradise for magnificent starbursts and rapid growth of supermassive black holes. In the local universe, the majority of the ultraluminous infrared galaxies (ULIRGs) are mergers of gas-rich galaxies. The merger process drives the gas and dust to the central region of the system, fueling the (circum)nuclear starbursts and the rapid accretMAion of the supermassive black holes. As described by a popular evolution scenario, the merger system advances from the ULIRG phase to the dusty quasar phase, and then to a fully exposed quasar phase, with the gas and dust either transformed into stars or expelled and/or heated by the galactic winds triggered by the quasar and starburst activities (e.g., Sanders et al. 1988; Veilleux et al. 2009a; Hickox & Alexander 2018). The ubiquity of galactic winds in local ULIRGs, dusty quasars, and luminous post-starburst galaxies supports this scenario. The observed winds extend over a large physical scale, from fast, nuclear winds on $\lesssim$pc scales all the way to galactic winds reaching $\gtrsim$10 kpc, blending smoothly with the circumgalactic medium (e.g., Martin 2005, 2006; Rupke et al. 2005; Tremonti et al. 2007; Martin & Bouché 2009; Sturm et al. 2011; Rupke & Veilleux 2013a; Veilleux et al. 2013a, 2013b, 2014, 2020; Cicone et al. 2014; Tombesi et al. 2015; Rupke et al. 2017; Fluetsch et al. 2019; Liu et al. 2019; Fluetsch et al. 2021; Lutz et al. 2020, for a review).

While the cooler, neutral, and/or molecular phases on larger scales ($\gtrsim$kpc) often dominate the outflow energetics, it is the hotter, ionized phase of the wind that serves as the best probe for the driving mechanism of these winds. ULIRG F11119+3257, arguably the best example so far, possesses a massive, galactic-scale (1–10 kpc) molecular and neutral-gas outflow apparently driven by the fast (>0.1 c), highly ionized (Fe XXV and Fe XXVI at ~7 keV) nuclear wind (Tombesi et al. 2015, 2017; Veilleux et al. 2017). While this result is intriguing, the faintness of the majority of ULIRGs at ~7 keV, unlike many quasars, has impeded a statistically meaningful study of this phenomenon in most ULIRGs with current X-ray facilities.

The superb far-ultraviolet (FUV) sensitivity of the Cosmic Origins Spectrograph (COS) on the Hubble Space Telescope (HST) provides a powerful alternative tool for such study in the low-z universe. Rest-frame FUV spectroscopy has enabled a comprehensive study of the multiphase nature of outflows, built upon the abundant spectral features arising from the high-ionization, low-ionization, and neutral phases of the outflowing gas (e.g., Tripp et al. 2011; Chisholm et al. 2015; Heckman et al. 2015; Hamann et al. 2019; Arav et al. 2020). Up to now, only about a dozen ULIRGs have been studied with HST/COS data, but the results are fascinating. In Mrk 231, highly blueshifted

Lyα emission (with respect to systemic velocity) is observed to coincide in velocity with the highly blueshifted absorption features tracing the fast outflow in this galaxy, suggesting an outflow-related origin for the Lyα emission (Veilleux et al. 2013a, 2016). With a larger sample of 11 ULIRGs, Martin et al. (2015, hereafter M15) have shown that prominent, blueshifted Lyα emission down to -1000 km s^{-1} exists in about half of the objects, and they argue that the blueshifted Lyα emission originates from the clumps of gas condensing out of hot winds driven by the central starbursts (Thompson et al. 2016). In addition, blueshifted absorption features from high-ionization species like O^{5+} and/or N^{4+} (114 and 77 eV are needed to produce these ions, respectively) and low-ionization species like Si^{+} and Fe^{+} are also detected in a few objects, providing unambiguous evidence of outflowing gas.

Despite the tantalizing evidence of FUV-detected outflows in the ULIRGs described above, the sample examined so far is small and incomplete, and AGN-dominated ULIRGs and matched quasars are largely missing. To address this issue, we have selected a more complete sample of ULIRGs and quasars to systematically study the gaseous environments along the merger sequence, from ULIRGs to quasars. In Veilleux et al. (2022; hereafter Paper I), we presented the results from the first part of our study, focused on the highly ionized gas outflows, traced by O VI 1032, 1038 and N V 1238, 1243 absorption features, in a sample of 33 local quasars. We found that the O VI and N V outflows are present in $\sim$61% of the sample, and the incidence rate and equivalent widths (EWs) of these highly ionized outflows are higher among X-ray weak or absorbed sources. Similarly, the flux-weighted outflow velocity dispersions are also the highest among the X-ray weakest sources. However, no significant correlation is visible between the flux-weighted outflow velocities/velocity dispersions and the other properties of the quasars and host galaxies.

In this paper, we report the results from an analysis of the Lyα emission and O VI and N V absorption features of the 21 ULIRGs in the sample,[7] expanding on the results from Paper I by considering the combined ULIRG+quasar sample. In Section 2, we describe the HST/COS observations of the ULIRG sample, the reduction of the data sets, and the ancillary data from the literature. In Section 3, we present the analysis of the FUV spectra of the ULIRGs, focusing on Lyα emission in the first part and the O VI and N V absorption features in the second. In Section 4, we discuss the potential key factors that control the observed Lyα properties, and in Section 5, we examine the incidence rates and properties of the O VI and N V outflows. In Section 6, we search for trends between the O VI and/or N V outflow properties and the AGN/galaxy properties in the ULIRG+quasar sample. In Section 7, we summarize the main results of this paper. Throughout the paper, we adopt a ΛCDM cosmology with $H_0 = 75$ km s^{-1} Mpc^{-1}, $\Omega_m = 0.3$, and $\Omega_\Lambda = 0.7$.

2. HST and Ancillary Data on the ULIRGs

2.1. HST/COS G130M Observations of ULIRGs

Our sample is selected based on three criteria: (1) They are part of the 1 Jy sample of 118 local ULIRGs with $z < 0.3$ and $|b| > 30^\circ$ (hence the modest Galactic extinctions; Kim & Sanders 1998). (2) In order to address the role of AGN feedback in these systems, the ULIRGs have AGN signatures in the optical (AGN Type 1 or 2) or in the mid-infrared (Spitzer-derived AGN bolometric fraction $\gtrsim$40%; Veilleux et al. 2009a). (3) They are the FUV-brightest ULIRGs of the 1 Jy sample with FUV magnitudes (AB) $m_{FUV} \lesssim 21$. These criteria result in a sample of 21 objects (Table 1): 15 of these objects were observed through the HST cycle 26 program (PID:15662; PI: Sylvain Veilleux), and the remaining six have archival COS G130M spectra of sufficient quality from three programs (PID: 12533, PI: C. Martin; PID: 12569, PI: S. Veilleux; PID: 12038: PI: J. Green). Among these six objects, QSO-B0157+001, 3C 273, and Mrk 231 were also studied in Paper I because they meet the criteria for QUEST quasars, and F01004−2237, Z11598−0112, and F12072−0444 were also studied in M15. In the following sections, we adopt the short names listed in Table 1 when referring to the objects in our sample.

The Cycle 26 HST/COS spectra presented in this paper were obtained in TIME-TAG mode through the PSA using the medium-resolution FUV grating, G130M. Four focal plane offset positions were adopted to reduce the impact of fixed-pattern noise associated with the microchannel plate. We got all four FP-POS settings for all targets, except for targets F04103, F14070, F21219, and F23233 with a central wavelength of 1291 Å. For these objects, we followed the COS2025 recommendations and used FP-POS = 3 and 4 to get equal exposures for segments A and B. The wavelength setting was adjusted according to the redshift of the target, and was selected to optimize the number of strong lines that can be observed with G130M. At all but the highest redshifts ($z < 0.2$), Lyα, the high-ionization lines from N V, and low-ionization lines from Si II 1260 and Si III 1206 fit within the wavelength coverage of the data. At the highest redshifts ($z \simeq 0.20$–0.27), we lose N V and Lyα but gain Lyβ and O VI 1032, 1038. The wavelength coverage for individual observations is summarized in Table 2.

2.2. HST/COS Data Reduction

Among the six objects with archival data, we retrieved the fully reduced spectra for five of them from the Hubble Legacy Spectrum Archive (Peeples et al. 2017), and obtained the fully reduced spectrum of F12072−0444 published in M15 from C. L. Martin. For the other 15 newly observed objects presented in this paper, the raw data were processed and combined by the CALCOS pipeline v3.3.10. CALCOS corrects the data for instrumental effects, assigns a vacuum wavelength scale, and extracts flux-calibrated spectra. It applies a heliocentric correction to the final $\times$1d files for each exposure, and combines the individual exposures to a single spectrum when possible.

The COS aperture is filled with emission from geocoronal airglow, so the observed wavelengths of these lines are independent of target position in the PSA. By inspecting the velocity offsets of theoretical and observed wavelength of strong geocoronal lines, we can examine the potential systematic errors in the wavelength calibration. The measured velocity offsets are randomly distributed with absolute values $<$30 km s^{-1}, and we take these measurements as typical errors of the wavelength calibration from the pipeline.

Finally, all spectra are corrected for foreground Galactic extinctions from Schlafly & Finkbeiner (2011) and the reddening curve with $R_V = 3.1$ of Fitzpatrick (1999).

[7] While FUV studies analyze Si IV and C IV transitions along with the lines of O VI and N V, our spectra do not cover the Si IV and C IV doublets at the target redshifts.

Table 1
Basic Properties of the ULIRGs in the Sample

Name	Short Name	z	log-$\left(\frac{L_{\rm bol}}{L_\odot}\right)$	Spectral Type	Merger Class	AGN Fraction	$m_{\rm FUV}$ (AB)	log(SX) (erg s^{-1})	log(HX) (erg s^{-1})	N_H(X-ray) (10^{22} cm^{-2})	log(λL_{1125})	$\alpha_{UV,X}$
(1)	(2)	(3)	(4)	(5)	(6)	(7)	(8)	(9)	(10)	(11)	(12)	(13)
F01004−2237	F01004	0.117701[a]	12.36	HII	V	55	18.5	41.0	42.1	...	44.2	−3.0
QSO-B0157+001	Mrk 1014	0.16311[b]	12.70	S1	IVb	73^{+24}_{-27}	16.6	43.92 ± 0.04	$43.83^{+0.11}_{-0.25}$	<0.009	45.3	−1.2
...	...	...	...	...	...	...	...	$44.00^{+0.04}_{-0.08}$	$43.86^{+0.04}_{-0.04}$	<0.009	...	...
F04103−2838	F04103	0.117464[b]	12.30	L	IVb	49	20.2	41.8	42.1	0.190	42.6	−1.4
F05189−2524	F05189	0.04288[c]	12.22	S2	IVb	71	19.1	43.4	43.4	7.83	42.8	−1.1
F07599+6508	F07599	0.1483[c]	12.58	S1	IVb	75	17.6	43.5	42.9	52.2	...	−2.5
F08572+3915:NW	F08572	0.0584[d]	12.22	L	IIIb	72	19.1	40.0	41.4	2.40	42.0	−3.4
F11119+3257	F11119	0.189[e]	12.64	S1	IVb	80	21.4	44.2	44.2	1.71	...	0.1
Z11598−0112	Z11598	0.150694[a]	12.49	S1	IVb	74	17.9	43.6	43.1	...	44.6	−0.9
F12072−0444	F12072	0.128360[a]	12.45	S2	IIIb	65	20.5	41.4	41.2	<0.01	42.9	−1.8
3C 273	3C 273	0.158339[b]	13.03	S1	IVb	95^{+5}_{-13}	13.3	$45.491^{+0.002}_{-0.002}$	$45.742^{+0.008}_{-0.008}$	<0.01	46.5	−0.9
...	...	...	...	...	...	...	...	$45.461^{+0.004}_{-0.004}$	$45.722^{+0.005}_{-0.006}$	<0.01	...	...
...	...	...	...	...	...	...	...	$45.591^{+0.002}_{-0.002}$	$45.820^{+0.004}_{-0.005}$	<0.01	...	...
...	...	...	...	...	...	...	...	$45.663^{+0.002}_{-0.001}$	$45.825^{+0.006}_{-0.006}$	<0.01	...	...
...	...	...	...	...	...	...	...	$45.461^{+0.003}_{-0.004}$	$45.67^{+0.01}_{-0.02}$	<0.01	...	...
...	...	...	...	...	...	...	...	$45.544^{+0.003}_{-0.003}$	$45.941^{+0.010}_{-0.007}$	<0.01	...	...
Mrk 231	Mrk 231	0.0422[c]	12.61	S1	IVb	71^{+7}_{-7}	19.0	$42.13^{+0.01}_{-0.04}$	$42.58^{+0.01}_{-0.11}$	$9.5^{+2.3}_{-1.9}$	42.7	−1.3
...	...	...	...	...	...	...	...	...	...	$19.4^{+5.7}_{-4.4}$	...	...
F13218+0552	F13218	0.2047[c]	12.68	S1	V	83	19.4	42.2	42.7	0.17	43.8	−2.0
F13305−1739	F13305	0.148365[b]	12.27	S2	V	88	19.5	...	...	...	...	...
Mrk 273	Mrk 273	0.03778[b]	12.24	S2	IVb	46	18.6	42.7	43.0	41.3	42.0	−1.6
F14070+0525	F14070	0.26438[b]	12.84	S2	V	41	21.0	...	...	...	...	...
F15001+1433:E	F15001	0.162746[b]	12.51	S2	Tpl	43	20.3	...	...	...	...	...
F15250+3608	F15250	0.05515[b]	12.12	L	IVa	45	18.5	43.1	42.8	132	42.7	−2.3
F16156+0146:NW	F16156	0.132[e]	12.19	S2	IIIb	77	20.9	...	...	...	...	...
F21219−1757	F21219	0.1127[c]	12.17	S1	V	78	17.3	...	...	...	44.7	...
F23060+0505	F23060	0.173[e]	12.50	S2	IVb	75	20.2	...	...	...	...	...
F23233+2817	F23233	0.114009[b]	12.06	S2	Iso	72	20.9	...	...	...	41.0	...

Notes. Column (1): Name of the object. Column (2): Short names of the objects adopted in this paper. Column (3): Redshift. The label on the upper right corner of each entry indicates the reference of the redshift.
[a] Based on the narrow optical emission lines from Martin et al. (2015).
[b] The best redshift adopted by NASA/IPAC Extragalactic Database (The NASA/IPAC Extragalactic Database (NED) is operated by the Jet Propulsion Laboratory, California Institute of Technology, under contract with the National Aeronautics and Space Administration.).
[c] Based on the narrow optical emission lines from Rupke et al. (2017).
[d] Based on the narrow optical emission lines from Rupke & Veilleux (2013b).
[e] Based on the optical emission lines from Kim & Sanders (1998). Column (4): Log of bolometric luminosity in solar units based on. For ULIRGs, we assumed $L_{\rm bol} = 1.15\ L_{\rm IR}$, where $L_{\rm IR}$ is the 8–1000 μm infrared luminosity from Kim & Sanders (1998). For the QUEST quasars, we assumed $L_{\rm bol} = 7$ L(5100 Å) + $L_{\rm IR}$ based on Netzer et al. (2007). Column (5): Optical spectral type from Veilleux et al. (1999), where S1 means Seyfert 1, S2 means Seyfert 2, L means LINER, and HII means star-forming. Column (6): Interaction class from Veilleux+02, where I = First approach, II = First contact, III(a/b) = Pre-merger (Wide binary/Close binary), IV(a/b) = Merger (Diffuse/Compact), V = Old Merger, Iso = Isolated, and Tpl = Triplet. Column (7): Fraction (in percentage) of the bolometric luminosity produced by the AGN, based on the mean values derived in Veilleux et al. (2009b). The typical uncertainties are 10%–15%. Column (8): FUV AB magnitudes from GALEX. Column (9): Soft (0.5–2 keV) X-ray luminosity. For X-ray related quantities (Column (9), (10), (11) and (13)), different rows = different observations dates. The references for these quantities are described in Section 2.3.2. The errors are omitted whenever they are not available from the literature or public data. Column (10): Hard (2–10 keV) X-ray luminosity. Column (11): The X-ray absorbing column density in units of 10^{22} cm^{-2}. Column (12): Monochromatic continuum luminosity at the rest-frame 1125 Å. Column (13): X-ray-to-UV index, $\alpha_{UV,X}$, as defined in Section 2.3.2.

Table 2
Summary of the HST/COS G130M Observations

Name (1)	PID (2)	PI (3)	Date (4)	R.A. (5)	Decl. (6)	Wavelength Coverage (7)	t_{exp} (8)
F01004	12533	C. Martin	2011-12-3	01 02 49.9631	−22 21 57.02	1137-1274/1292-1432	1716
Mrk 1014	12569	S. Veilleux	2012-1-25	01 59 50.250	+00 23 41.30	1154-1468	1961
F04103	15662	S. Veilleux	2020-1-23	12 19.413	−28 30 24.64	1137-1274/1292-1432	10798
F05189	15662	S. Veilleux	2019-7-18	05 21 01.388	−25 21 45.10	1069-1207/1223-1363	7802
F07599	15662	S. Veilleux	2019-2-21	04 30.487	+64 59 52.75	1173-1312/1328-1468	2148
F08572	15662	S. Veilleux	2019-10-17	00 25.281	+39 03 54.83	1069-1207/1223-1363	7906
F11119	15662	S. Veilleux	2020-1-20	14 38.908	+32 41 33.04	1173-1312/1328-1468	13537
Z11598	12533	C. Martin	2011-11-18	12 02 26.7505	−01 29 15.49	1154-1468	1304
F12072	12533	C. Martin	2013-1-24	12 09 45.1000	−05 01 13.20	1137-1448	1176
3C 273	12038	J. Green	2012-4-22	12 29 06.695	+02 03 08.66	1137-1408	4515
Mrk 231	12569	S. Veilleux	2011-10-15	12 56 14.111	+56 52 24.70	1154-1468	12851
F13218	15662	S. Veilleux	2020-5-21	24 19.897	+05 37 05.06	1069-1207/1223-1363	7742
F13305	15662	S. Veilleux	2019-12-17	33 16.529	−17 55 10.52	1173-1312/1328-1468	7776
Mrk 273	15662	S. Veilleux	2019-7-23	13 44 42.080	+55 53 12.99	1069-1207/1223-1363	4086
F14070	15662	S. Veilleux	2020-6-30	09 31.249	+05 11 31.45	1137-1274/1292-1432	13377
F15001	15662	S. Veilleux	2020-3-1	02 31.936	+14 21 35.15	1173-1312/1328-1468	10719
F15250	15662	S. Veilleux	2019-7-11	26 59.463	+35 58 37.47	1069-1207/1223-1363	4951
F16156	15662	S. Veilleux	2020-7-8	18 09.426	+01 39 21.66	1173-1312/1328-1468	13346
F21219	15662	S. Veilleux	2019-4-13	24 41.606	−17 44 45.52	1137-1274/1292-1432	2210
F23060	15662	S. Veilleux	2019-12-5	08 33.947	+05 21 29.95	1173-1312/1328-1468	10703
F23233	15662	S. Veilleux	2019-10-14,2020-1-2223	25 49.406	+28 34 20.84	1137-1274/1292-1432	13477

Note. Column (1): Name of the object. Column (2): HST Program ID. Column (3): Principal Investigator. Column (4): Date of Observation. Column (5) & (6): J2000 coordinates. Column (7): Wavelength coverage of the observations in Å. The values are formatted as A/B segments or entire wavelength ranges. Column (8): Total exposure time in seconds.

2.3. Ancillary Data and Measurements

2.3.1. General Physical Properties

For the bolometric luminosities of our sources, we adopt $L_{bol} = 1.15\ L_{IR}$, where L_{IR} is the 8–1000 μm infrared luminosity retrieved from Kim & Sanders (1998), except for the three sources that are also QUEST quasars, which are quoted from Paper I, where we assume $L_{bol} = 7\ L(5100\ \text{Å}) + L_{IR}$ based on Netzer et al. (2007). The L(5100 Å) is the continuum luminosity λL_λ at 5100 Å rest wavelength, and L_{IR} is the 1–1000 μm infrared luminosity (the details can be found in the notes of Table 1 in Paper I).

The optical spectral classifications are quoted from Veilleux et al. (1999): S1 means Seyfert 1, S2 means Seyfert 2, L means LINER, and HII means star-forming galaxies. The interaction classes (or merger classes) are from Veilleux et al. (2002): I—First approach, II—First contact, III(a/b)—Pre-merger (Wide binary/Close binary), IV(a/b)—Merger (Diffuse/Compact), V—Old Merger, Iso—Isolated, and Tpl—Triplet. The fraction of the bolometric luminosity produced by the AGN, or simply AGN fractions, are the average values derived in Veilleux et al. (2009a). The AGN luminosities are defined as the bolometric luminosities multiplied by the AGN fractions.

2.3.2. X-Ray Data

Published X-ray data and measurements exist for 14 out of the 21 objects: Those for the three quasars (QSO-B0157+001, 3C 273, Mrk 231) also studied in Paper I are from Teng & Veilleux (2010), Teng et al. (2014), Veilleux et al. (2014), and Ricci et al. (2017). Those for the remaining 11 sources are from a series of X-ray studies of ULIRGs and quasars (Teng et al. 2005; Teng & Veilleux 2010).

Following Paper I, the X-ray weakness of AGN/quasars can be described with the X-ray to optical spectral index, $\alpha_{OX} \equiv 0.372 \log[(F(2\ \text{keV})/F(3000\text{Å})]$ (e.g., Brandt et al. 2000). While α_{OX} is measured for most nearby quasars, there are virtually no published measurements for the ULIRGs in our sample. Instead, we have defined an alternative X-ray to FUV spectral index, $\alpha_{UV,X}$, based on the ratio of the soft X-ray (0.5–2 keV) flux to the FUV flux from GALEX (Martin et al. 2005), where $\alpha_{UV,X} \equiv \log[F(0.5\text{–}2\ \text{keV})/F(FUV)]$. These results are listed in Table 1.

For the QUEST quasars studied in Paper I, there is a clear positive correlation between $\alpha_{UV,X}$ and α_{OX} (see Figure 1), with a p-value $\simeq 2 \times 10^{-5}$ from the Kendall tau test (the null hypothesis is no correlation), which demonstrates that $\alpha_{UV,X}$ is indeed a good surrogate for α_{OX}. For the quasars without published 0.5–2 keV flux from Chandra or XMM-Newton and/or FUV flux from GALEX, we convert their α_{OX} listed in Paper I to $\alpha_{UV,X}$ by adopting the relation $\alpha_{UV,X} = 2.17\ \alpha_{OX} + 2.26$, which is obtained from a linear fit to the quasars with both $\alpha_{UV,X}$ and α_{OX} measurements.

2.3.3. Optical Spectra

The Gemini/GMOS IFU spectra from Rupke & Veilleux (2013b), Rupke et al. (2017), or the SDSS spectra (Eisenstein et al. 2011) are adopted as the optical spectra for our objects by default unless explicitly stated otherwise (the GMOS data are adopted by default whenever both GMOS and SDSS data are available for the same object). The long-slit, optical spectra of all objects but 3C 273 are retrieved from Veilleux et al. (1999), and the optical spectrum of 3C 273 is retrieved from Buttiglione et al. (2009). They are adopted as the default optical spectra whenever the Gemini/GMOS and SDSS spectra are not available.

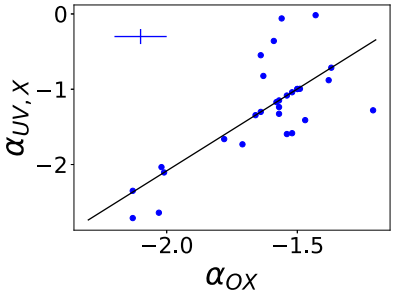

Figure 1. The X-ray to optical spectral index α_{OX} vs. the X-ray to FUV spectral index $\alpha_{UV,X}$ for the quasars in Paper I. The two indices are defined as $\alpha_{OX} \equiv 0.372\log[F(2\text{ keV})/F(3000\text{Å})]$ and $\alpha_{UV,X} \equiv \log[F(0.5\text{–}2\text{ keV})/F(\text{FUV})]$, respectively. The solid line is a linear fit to the data points. The errors on α_{OX} and $\alpha_{UV,X}$ are uncertain, and largely associated with the uncertainties in the analyses of the X-ray spectra, as described in, e.g., Teng & Veilleux (2010). The cross in the upper left corner of the figure indicates ±0.1 dex errors adopted in the Kendall tau test and the fit.

For these spectra, the continua are modeled with either stellar population synthesis (SPS) models (González Delgado et al. 2005) adopting pPXF (Cappellari 2017) or fourth-order polynomials and/or power-law function with customized Python software utilizing LMFIT (Newville et al. 2016), on a case-by-case basis. The properties of the [O III] λ5007 and Hα emission lines are then measured from these continuum-subtracted optical spectra.

2.3.4. AGN Fractions of Starburst-dominated ULIRGs

Most of the key AGN and host galaxy properties of the QUEST quasars from Paper I and the starburst-dominated ULIRGs from M15 are tabulated in these papers. One exception is the AGN fractions of the ULIRGs in M15, which are estimated based on the IRAS-based 25 μm to 60 μm flux ratios (F25/F60) listed in Table 1 of M15. Specifically, the AGN fraction is calculated adopting the best fit to the trend presented in Figure 36(c) in Veilleux et al. (2009a):

$$f_{\rm AGN}(\%) = \begin{cases} 67.1x + 100.2, \; if \; x \geqslant -1.1 \\ \leqslant 27.3, \; if \; x < -1.1 \end{cases} \quad (1)$$

where $x = \log(F25/F60)$.

3. Results from the HST Data Analysis

In this section, we present the major results from our analysis of the HST/COS spectra. First, the properties regarding Lyα emission are examined in Section 3.1. Second, the measurement of FUV continuum luminosity is briefly described in Section 3.2, Finally, the properties of O VI 1032, 1038 and N V 1238, 1243 absorbers are discussed in Section 3.3.

3.1. Lyα Emission

3.1.1. Detection Rates

The Lyα transition falls within the wavelength range of the observations for 19 of the 21 objects. Among the 19 objects, the Lyα emission is detected (S/N > 3) in 15 of them, including F07599, where the Lyα emission is heavily affected by deep, broad, and narrow N V 1238, 1243 absorption features (and perhaps also broad Lyα absorption). After Lyα, N V 1238, 1243 and O VI 1032, 1038 are the most frequently detected emission lines in our sample (notice that our G130M spectra do not cover Si IV and C IV). Descriptions about the presence of emission/absorption features other than Lyα in our objects may be found in the Appendix.

3.1.2. Line Profiles

The Lyα profiles of the 15 Lyα detections are presented in Figure 2. For these objects, the Lyα emission is the most prominent feature in the observed spectral range, except for F07599, where the Lyα line is severely suppressed by a highly blueshifted broad absorption line (BAL) and several less blueshifted narrow N V 1238, 1243 absorption features. As a result, a relatively robust measurement of the Lyα profile of F07599 is impossible, and this source is omitted from the analyses to characterize the Lyα profiles in the following sections.

The flux and EWs of the entire Lyα profiles are measured in wavelength windows customized for each object based on their line widths. The local continuum of each object is determined by fitting the line-free windows adjacent to the Lyα features with power-law or low-order polynomials (order $\leqslant$2). The contamination from nearby N V emission is subtracted for sources Mrk 1014, F05189, 3C 273, and F21219, where the N V doublet are modeled as Gaussian profiles. The foreground absorption features and absorption lines from other species at the systemic velocity are interpolated over with cubic splines. For the nondetections, the 3σ upper limits on the flux of Lyα are estimated in a velocity window of -1000 to $+1000$ km s^{-1}.

We adopt a nonparametric approach to characterize the Lyα profiles quantitatively: the velocities v_{50} and v_{80} (velocities at 50% and 80% of the total flux calculated from the red side of the line), the line width W_{80} (which encloses the central 80% of the total flux), and the line asymmetry A_{91} ($[v_{90}+v_{10}]/W_{80}$), where v_{90} and v_{10} are the velocities at 90% and 10% of the total flux calculated from the red side of the line) are the primary measurements adopted for our analyses in the following sections. All velocities are calculated with respect to the systemic redshifts listed in Table 1. Table 3 summarizes the results. A visualization of these nonparametric measurements is shown in Figure 3.

Blueshifted wings of the Lyα emission are often seen across our sample (12 out of the 14 objects with robustly measured Lyα profiles show $v_{80} < 0$ and line asymmetry $A_{91} < 0$), while the P-Cygni-like profile (blueshifted absorption accompanied by redshifted emission) is only seen in F15250 (in F16156, a weak blueshifted wing is seen in the Lyα emission blueward of the strong blueshifted absorption feature, and the overall Lyα profile is thus not P-Cygni-like). This is in clear contrast with the prevalence of P-Cygni-like profiles seen in low-redshift star-forming galaxies (e.g., Wofford et al. 2013). The blueshift of the velocity centroid of the Lyα line is also prevalent in our sample, where 11 out of the 14 objects with Lyα detections show $v_{50} < 0$. Moreover, in two Type 1 sources, 3C 273 and Mrk 1014, the broad Lyα emission (accompanied by broad N V 1238, 1243 emission, when the spectrum covers this region) shows a line width typical for the broad emission line region (BELR) of AGN, which is often the case for low-redshift Type 1 AGN and quasars (e.g., Shull et al. 2012). Finally, Lyα absorption features near systemic velocities are clearly seen in nine objects.

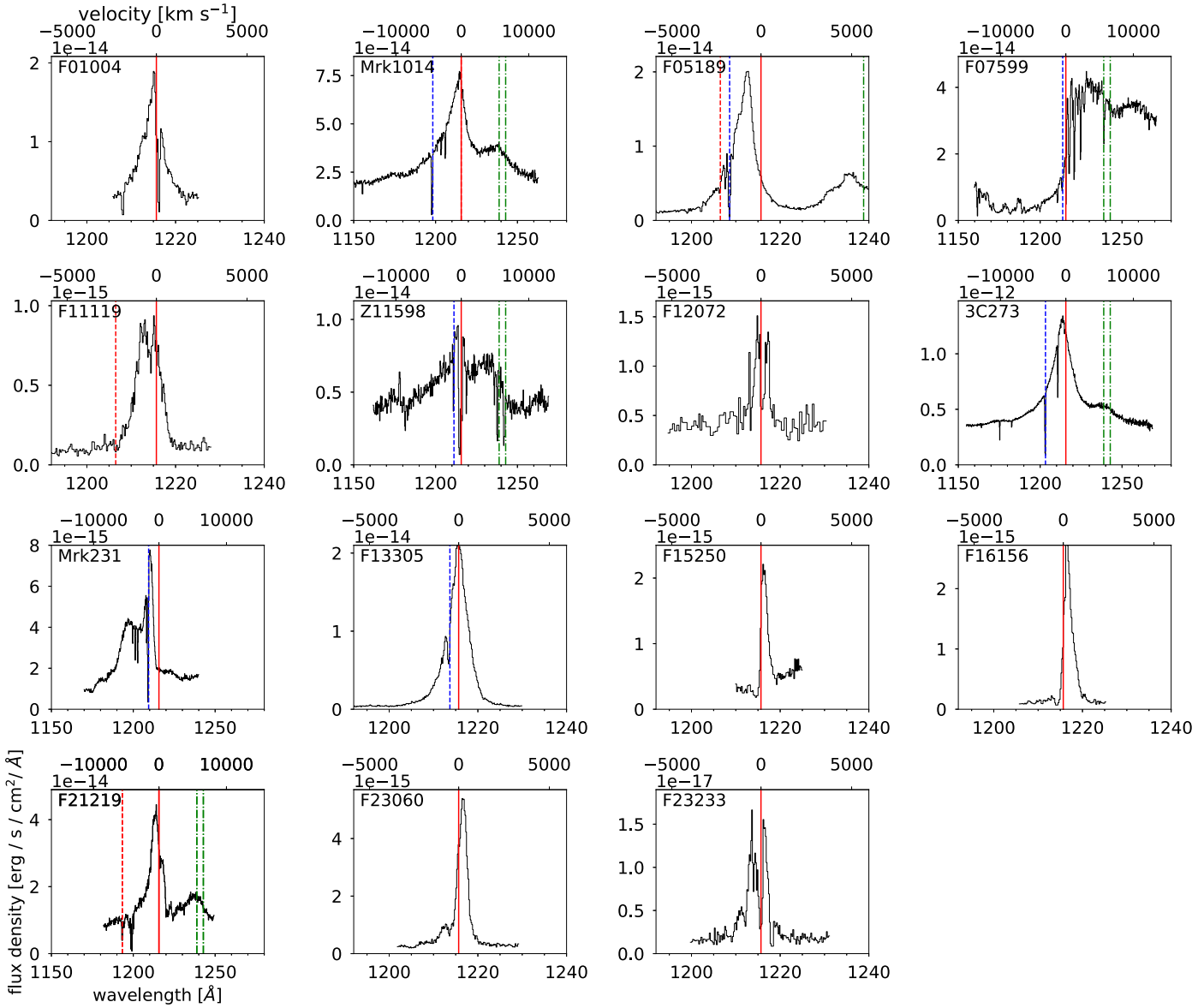

Figure 2. Lyα profiles of the 14 objects with clear Lyα emission and the one with a potential detection F07599. The spectra are shown in each object's rest frame. The velocities relative to the Lyα transition are shown on the top of each panel, and the zero velocities are indicated by the vertical solid lines. The zero velocities of the N V 1238, 1243 doublet are indicated by the vertical green dashed–dotted lines when they are blended with the Lyα emission. Other strong absorption features at the systemic velocities are indicated by vertical dashed lines in red. Foreground absorption features at $z \simeq 0$ due to the Milky Way are indicated by dashed lines in blue. The flux scale for the vertical axis in units of erg s^{-1} cm^{-2} Å^{-1} is listed in the upper left corner above each panel. To help with the visual comparison among different objects, the x-axes are set to two fixed wavelength ranges (1192–1240 Å or 1150–1280 Å) depending on the widths of the lines.

3.1.3. Comparison of the Lyα and Optical Emission Line Profiles

The observed Lyα profiles in these dusty ULIRGs are likely affected by complex radiative transfer effects due to the resonant nature of the transition. While it is impossible to derive the intrinsic profile of the resonant Lyα line with our data, the nonresonant optical emission lines (e.g., [O III] λ5007 forbidden line, Hα recombination line) provide a point of reference because they are less affected by absorption and scattering. Qualitatively, we may therefore infer the extent to which Lyα photons are absorbed and/or scattered, by comparing the Lyα and optical line profiles.

In Figures 4 and 5, we plot the Lyα profiles in comparison with the [O III] λ5007 profiles and the Hα profiles. All of these line profiles are continuum-subtracted and rescaled for better visualization. In total, 11 objects with [O III] λ5007 observations and 15 objects with Hα observations show Lyα detections. The measurements of the [O III] λ5007 and Hα profiles are summarized in Table 4. At first glance, one similarity between the Lyα profiles and the nonresonant line profiles is the occurrence of blueshifted emission line wings in many objects. Blueshifted [O III] λ5007 (and to a lesser extent, Hα) emission is a telltale signature of ionized gas outflows, so the blueshifted Lyα emission may also arise from the outflowing gas. In addition, Lyα emission is generally broader than or comparable in width to the [O III] λ5007 and Hα emission. Otherwise, the Lyα profiles are diverse among the objects in our sample and no apparent trend is seen between the profiles of Lyα and the nonresonant optical lines. We will discuss these results further in Section 4.2.

Table 3
Lyα Measurements

Name	log(Flux) (erg cm^{-2} s^{-1})	log(Lum.) (erg s^{-1})	EW (Å)	v_{50} (km s^{-1})	v_{80} (km s^{-1})	W_{80} (km s^{-1})	A_{91}	log(f_{esc}(Lyα))
(1)	(2)	(3)	(4)	(5)	(6)	(7)	(8)	(9)
F01004	-13.09 ± 0.02	42.48 ± 0.02	27.8 ± 4.7	-228 ± 42	-788 ± 78	1792 ± 51	-0.25 ± 0.14	0.12 ± 0.49
Mrk 1014	-11.74 ± 0.006	44.13 ± 0.006	102.7 ± 0.3	-1274 ± 153	-5453 ± 654	10876 ± 1305	-0.62 ± 0.12	-0.22 ± 0.32
F04103	<-14.07	<41.49	...	...	...	...	...	<-2.36
F05189	-12.79 ± 0.02	41.86 ± 0.02	164.0 ± 56.8	-913 ± 71	-1782 ± 159	2748 ± 50	-0.87 ± 0.22	-1.29 ± 0.30
F07599	...	...	...	...	...	...	...	...
F08572	<-12.86	<42.05	...	...	...	...	...	<-0.28
F11119	-14.17 ± 0.05	41.85 ± 0.05	80.8 ± 39.8	-467 ± 211	-1104 ± 245	2170 ± 548	-0.53 ± 0.97	-3.89 ± 0.32
Z11598	-12.65 ± 0.003	43.15 ± 0.003	70.5 ± 2.3	-1739 ± 591	-6517 ± 2216	12766 ± 4340	-0.51 ± 0.31	0.34 ± 0.44
F12072	-14.23 ± 0.07	41.41 ± 0.07	17.2 ± 10.2	-75 ± 100	-743 ± 150	1601 ± 122	-0.25 ± 0.65	-0.62 ± 0.07
3C 273	-10.67 ± 0.04	45.18 ± 0.04	53.0 ± 8.3	-624 ± 340	-2988 ± 792	7875 ± 10	-0.32 ± 0.53	-0.08 ± 0.36
Mrk 231	-13.08 ± 0.03	41.54 ± 0.03	53.2 ± 10.2	-2771 ± 371	-4731 ± 309	4698 ± 20	-1.34 ± 0.31	-2.64 ± 0.80
F13218	...	...	...	...	...	...	...	...
F13305	-12.72 ± 0.02	43.06 ± 0.02	307.1 ± 257.9	-20 ± 58	-599 ± 97	1775 ± 18	-0.15 ± 0.15	-0.19 ± 0.48
Mrk 273	<-12.85	<41.68	...	...	...	...	...	<-0.91
F14070	...	...	...	...	...	...	...	...
F15001	<-14.09	<41.78	...	...	...	...	...	<-0.80
F15250	-15.32 ± 0.11	39.55 ± 0.11	0.7 ± 18.0	394 ± 7	359 ± 7	112 ± 78	7.28 ± 5.09	-1.41 ± 0.37
F16156	-13.94 ± 0.06	41.73 ± 0.06	62.8 ± 66.8	331 ± 78	142 ± 85	749 ± 62	1.12 ± 2.33	-1.33 ± 0.34
F21219	-12.21 ± 0.02	43.31 ± 0.02	46.3 ± 4.0	-384 ± 86	-1488 ± 180	4036 ± 48	-0.20 ± 0.12	-0.81 ± 0.44
F23060	-13.57 ± 0.05	42.36 ± 0.05	90.4 ± 80.2	219 ± 69	-228 ± 201	1535 ± 89	-0.10 ± 1.06	-2.47 ± 0.36
F23233	-15.88 ± 0.06	39.65 ± 0.06	36.8 ± 18.2	-278 ± 188	-709 ± 166	1600 ± 582	-0.45 ± 1.20	-2.10 ± 1.10

Note. Column (2): Observed Lyα flux (cgs units) in logarithm. Column (3): Lyα luminosity (cgs units) in logarithm. Column (4): Lyα EW in units of Å. Column (5): v_{50} of Lyα profile in units of km s^{-1}. Column (6): v_{80} of Lyα profile in units of km s^{-1}. Column (7): W_{80} of Lyα profile in units of km s^{-1}. Column (8): A_{91} of Lyα. Column (9): Logarithm of Lyα escape fraction as defined in Section 3.1.4. Note that, for F13218 and F14070, the Lyα transition is not covered by the observations, while for F07599, the Lyα feature cannot be measured robustly, mainly due to contamination from the N V BAL.

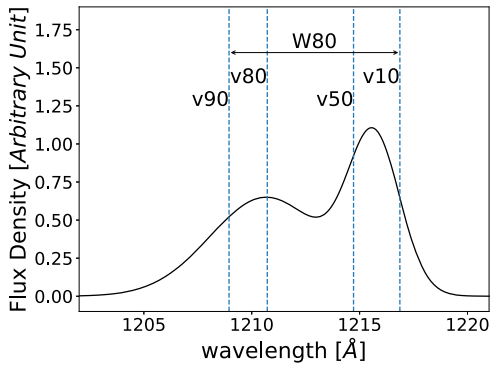

Figure 3. Example of a line profile illustrating the various nonparametric kinematic parameters used in this paper. The vertical dashed lines mark the locations of v_{90}, v_{80}, v_{50}, and v_{10} for the mock emission-line profile shown in the figure. W_{80} is defined as the line width between v_{90} and v_{10}, and the line asymmetry A_{91} is $[v_{90}+v_{10}]/W_{80}$ (not shown in the figure).

3.1.4. Lyα Escape Fraction

At first, it may be surprising that significant Lyα emission is observed from these dusty ULIRGs, given the implied huge optical depth to Lyα photons. In this section, we quantify the escape of Lyα photons by calculating the Lyα escape fraction.

Under Case B recombination, the ionized region is optically thick to the Lyman series, and the intrinsic F(Lyα)/F(Hα) flux ratio depends only on the electron density and temperature. Adopting the low density limit where $n_e \ll n_{e,\rm crit} = 1.55 \times 10^4\,{\rm cm}^{-3}$, the collisions can be safely neglected. The intrinsic Lyα flux is then predicted to be 8.1 times the intrinsic Hα flux (Hummer & Storey 1987; Draine 2011).

Galaxies usually show Lyα-to-Hα flux ratios much less than the predicted Case B ratio. We can therefore describe the suppression of Lyα photons by comparing the observed Lyα flux to the intrinsic values indicated by the Hα emission. The escape fraction of Lyα photons can thus be defined as

$$f_{\rm esc}\,({\rm Ly}\alpha) = \frac{F\,({\rm Ly}\alpha)}{8.1 \times F\,({\rm H}\alpha)_{\rm cor}}. \quad (2)$$

The intrinsic Hα flux is calculated from the observed Hα flux, corrected for the nebular reddening using the Cardelli et al. (1989) reddening curve, namely

$$F_{\rm cor}({\rm H}\alpha) = F_{\rm obs}({\rm H}\alpha) \times 10^{1.012E(B-V)}, \quad (3)$$

and the $E(B-V)$ is calculated from the Balmer decrement:

$$E(B-V) = \frac{1}{0.9692} \log\left[\frac{(F\,({\rm H}\alpha)/F\,({\rm H}\beta))_{\rm obs}}{(F\,({\rm H}\alpha)/F\,({\rm H}\beta))_{\rm int}}\right]. \quad (4)$$

We set the intrinsic Hα/Hβ ratio to 3.1 for all but one object, as they show optical spectral features consistent with AGN activity. The only exception is F01004: it is located in the star-forming region in the BPT and VO87 diagnostic line ratio diagrams (Baldwin et al. 1981; Veilleux & Osterbrock 1987; Osterbrock & Ferland 2006), and we set the intrinsic Hα/Hβ ratio of this object to 2.87.

The Hα fluxes are measured from spectra gathered from literature, as described in Section 2.3.3, and can be divided into three groups: (1) Gemini/GMOS IFU observations; (2) SDSS spectra; and (3) long-slit spectra from Veilleux et al. (1999). Some of our objects are point sources or show very compact morphology in the narrowband Hα images (based on the GMOS data) or *R*-band images (from SDSS or Veilleux et al. 1999), so

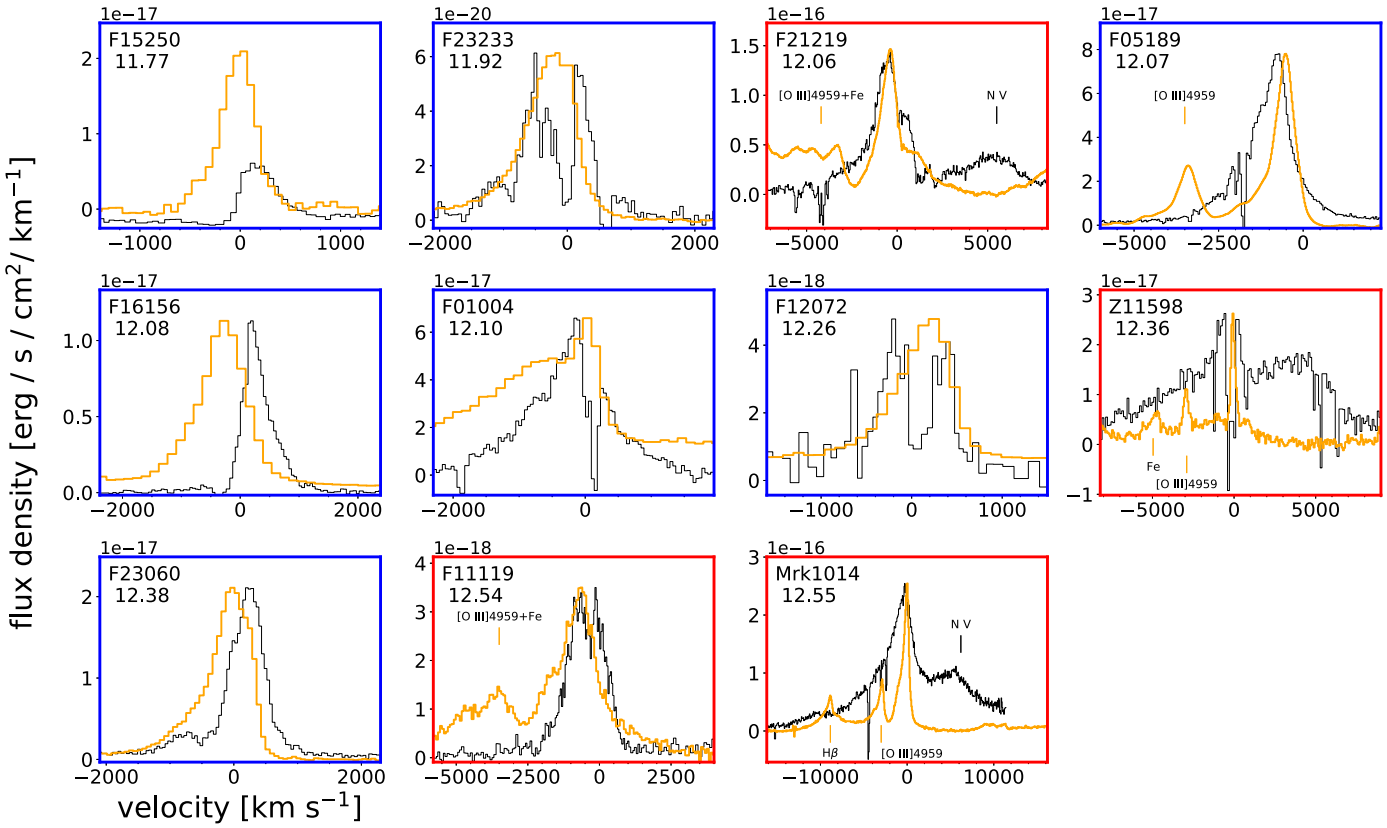

Figure 4. Comparison of Lyα profiles (black) with [O III] λ5007 emission lines (orange) for the 11 objects in our sample with both Lyα detections and [O III] λ5007 observations. The flux scale on the vertical axis refers to the Lyα line, and the scale factor in units of erg s^{-1} cm^{-2} km^{-1} s is listed in the upper left corner above each panel. The [O III] emission-line profiles are rescaled for better visualization. Nearby emission features from N V in the FUV and those from Hβ, [O III] λ4959, and Fe in the optical are marked with black and orange vertical bars, respectively, when those features are present. The panels are ordered by increasing AGN luminosities, which are indicated in the top left corner of each panel under the object name (in log units of solar luminosities). The panel frames of Type 1 AGN are marked in red, and those of type 2 AGN are marked in blue.

no aperture corrections are needed for their Hα flux in the calculation of Lyα escape fraction. However, for the more extended objects, the aperture difference between the COS FUV spectroscopy and the optical observations need to be taken into account, as the throughput of the 2.″5 COS aperture drops sharply beyond the central 0.″4.

In practice, the aperture correction is negligible if at least one of the following three criteria is met: (1) it is a Type 1 AGN; (2) the PSF contribution to its overall flux in the *R*-band image is more than 50% based on the measurements in Veilleux et al. (2002); or (3) the *R*-band effective radius is less than 1″ based on the measurements in Veilleux et al. (2002). For the other objects, aperture corrections are needed to account for the rapid decrease of COS throughput at large radius as mentioned above. Specifically, we calculate the aperture correction factors for each group of optical observations separately: (i) For the GMOS IFU observations, we generate the Hα flux maps based on the data cube, and use the COS throughput function to vignette the Hα flux maps within the region with radius $r < 1.''25$. The aperture correction factor is then the vignetted Hα flux within $r < 1.''25$ (corresponding to the COS aperture) divided by the original Hα flux within the same aperture. (ii) For the SDSS spectra, we adopt the *r*-band images as surrogates for the Hα flux maps. We then vignette the *r*-band images within the same COS throughput function, and the aperture correction factor is the vignetted *r*-band flux within r $< 1.''25$ divided by the original *r*-band flux within SDSS aperture ($D = 3''$ or $D = 2''$). (iii) For the long-slit spectra from Veilleux et al. (1999), we follow the same logic as adopted for the SDSS spectra, but use the *R*-band images in Kim et al. (2002). The aperture correction factor is thus the vignetted *R*-band flux within $r < 1.''25$ divided by the original *R*-band flux within the extraction region of the long-slit spectra ($2'' \times 5''$ kpc).

The aperture correction factors adopted in the calculations and resulting Lyα escape fractions are listed in Tables 4 and 3, respectively.

3.2. Continuum Luminosity at 1125 Å

As a surrogate for the FUV continuum luminosity adopted in Paper I, the monochromatic luminosities at rest-frame 1125 Å, log(λL_{1125}), are measured whenever the continuum is detected, with a bandpass of 20 Å. These results are recorded in Table 1.

3.3. FUV Absorption Features

The focus of this section is the strongest metal absorption features detected in our objects, O VI 1032, 1038 and N V 1238, 1243, tracers of the highly ionized gas in these systems. Only 12 out of the 21 objects have continuum S/N in the vicinity of O VI 1032, 1038 and/or N V 1238, 1243 that are high enough (S/N $\gtrsim$ 10 in a 500 km s^{-1} window) to allow for the detection of corresponding absorption lines. Out of these 12 objects, six show O VI and/or N V absorption features associated with the

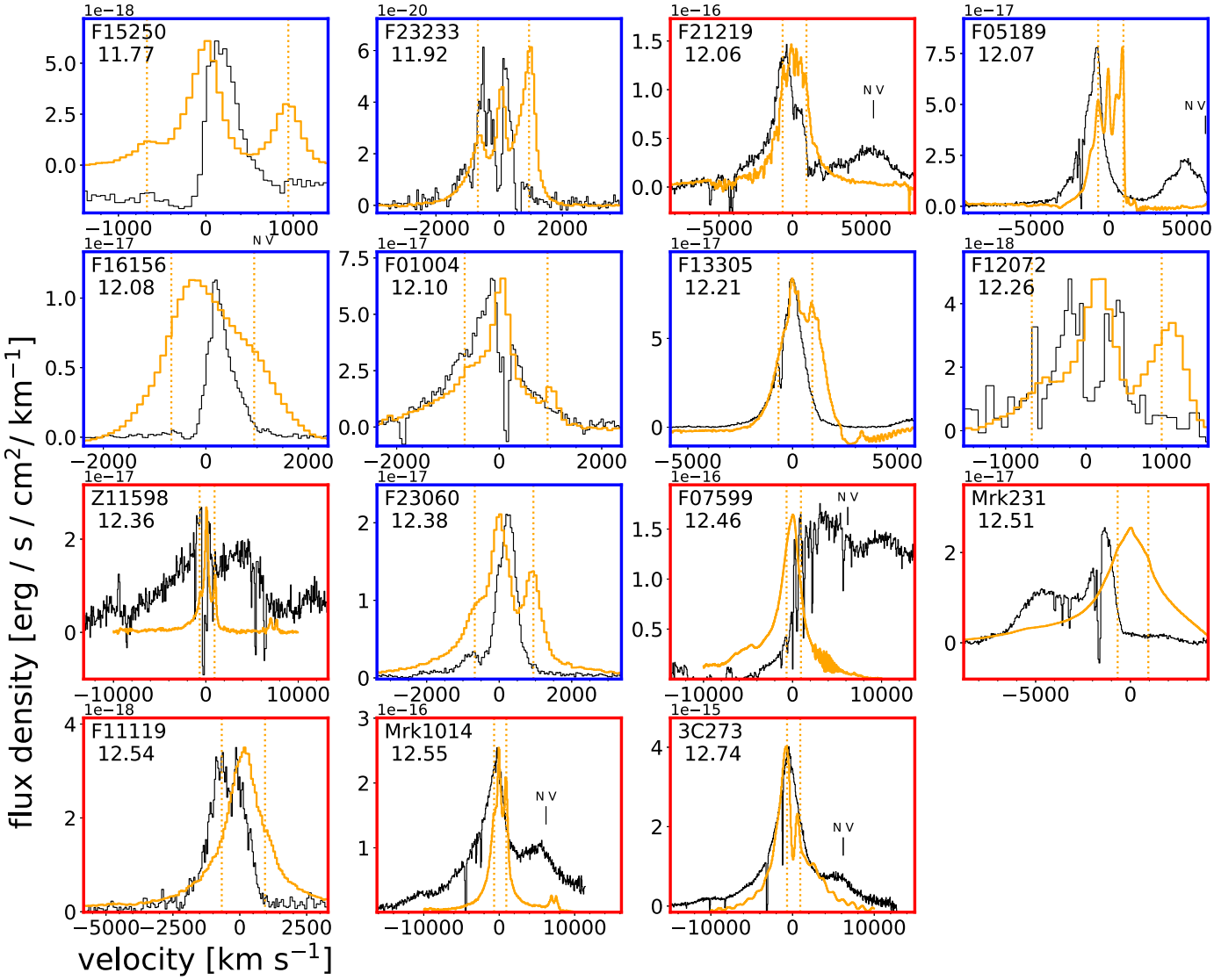

Figure 5. Same as Figure 4, but for the comparison of the Lyα (black) and Hα (orange) emission lines for the 15 objects with Lyα detections. The nearby N V emissions are marked with black bars when those features are present. Note that, in some cases, the strong [N II] $\lambda\lambda$6548, 6583 emission lines in the optical near -674 km s^{-1} and $+944$ km s^{-1} (marked by orange dotted lines) make this comparison difficult.

galaxy (velocity centroid <13,000 km s^{-1} and not from intervening systems), and the velocity centroids of these absorption features are all blueshifted. One more object, F15250, may display a N V absorption feature, but the doublet is so close to a group of geocoronal emission lines that the N V 1239 transition is heavily contaminated and no robust measurements of the N V feature can be made. Our estimates for the EW and centroid velocity of the N V 1242 absorber alone are $\sim$0.3 Å and -500 km s^{-1}, respectively, without taking into account the infilling from the N V 1238, 1243 emission. This source is excluded from the discussions related to the absorption features in the following sections.

The properties of these detected O VI and/or N V absorption features vary wildly: F07599 shows a >25,000 km s^{-1} wide N V 1238, 1243 BAL accompanied by narrower absorbers at smaller velocities, whereas F23060 shows relatively narrow and shallow N V 1238, 1243 absorption features on top of the N V 1238, 1243 emission. Overall, the absorption features in F07599 and F01004 fall in the BAL category (velocity width >2000 km s^{-1}), while all other absorption features are classified as narrow absorption lines (NAL; velocity width <500 km s^{-1}). An object-by-object description of these absorption features is given in the Appendix.

To quantify the strength of these absorbers, we follow the same procedure as in Paper I. First, we fit the continuum and/or broad emission lines (Lyα, O VI, and N V) with low-order polynomials or Gaussian profiles. After the spectra are normalized by the best fits from the continuum and/or broad emission line fits, these absorbers are quantified using a nonparametric approach, where we measure the total velocity-integrated EWs of the outflowing absorbers in the object's rest frame,

$$W_{\rm eq} = \int [1 - f(\lambda)] d\lambda, \quad (5)$$

the weighted average outflow velocity,

$$v_{\rm wtavg} = \frac{\int v[1 - f(v)] dv}{W_{\rm eq}}, \quad (6)$$

Table 4
Optical Spectroscopic Measurements

Name	$E(B-V)$	log(Flux(Hα)) (erg cm^{-2} s^{-1})	cor,Hα	$v_{50,\mathrm{H}\alpha}$ (km s^{-1})	$v_{80,\mathrm{H}\alpha}$ (km s^{-1})	$W_{80,\mathrm{H}\alpha}$ (km s^{-1})	$A_{91,H\alpha}$	$v_{50,[\mathrm{O\ III}]}$ (km s^{-1})	$v_{80,[\mathrm{O\ III}]}$ (km s^{-1})	$W_{80,[\mathrm{O\ III}]}$ (km s^{-1})	$A_{91,[O\ \mathrm{III}]}$
(1)	(2)	(3)	(4)	(5)	(6)	(7)	(8)	(9)	(10)	(11)	(12)
F01004	0.05 ± 0.004	-14.05 ± 0.03	0.86	111 ± 100	-688 ± 100	1398 ± 141	-0.54 ± 0.11	-563 ± 199	-1560 ± 200	2591 ± 282	-0.58 ± 0.13
Mrk 1014	0.24 ± 0.02	-12.42 ± 0.04	0.98	113 ± 69	-1061 ± 69	4901 ± 98	0.19 ± 0.02	-147 ± 69	-768 ± 69	1519 ± 98	-0.42 ± 0.07
F04103	1.29 ± 0.13	-12.54 ± 0.03	0.82	...	...	...	...	...	...	...	...
F05189	1.02 ± 0.10	-12.34 ± 0.04	0.86	-354 ± 20	-904 ± 20	1588 ± 29	-0.90 ± 0.02	-661 ± 27	-1195 ± 27	1415 ± 38	-1.38 ± 0.05
F07599	...	-10.03 ± 0.03	0.68	642 ± 3760	323 ± 4079	957 ± 5393	1.48 ± 10.06	...	...	...	...
F08572	...	-13.36 ± 0.03	0.75	...	...	...	...	...	...	...	...
F11119	...	-11.19 ± 0.03	1.00	144 ± 69	-1029 ± 69	4970 ± 98	0.00 ± 0.02	-667 ± 69	-1427 ± 69	2278 ± 98	-0.62 ± 0.05
Z11598	...	-13.69 ± 0.03	0.62	172 ± 69	-1071 ± 69	4901 ± 98	-0.38 ± 0.02	-64 ± 60	-1734 ± 60	4057 ± 84	-0.31 ± 0.02
F12072	0.10 ± 0.001	-14.80 ± 0.001	1.33	49 ± 87	-213 ± 88	1051 ± 124	-0.03 ± 0.12	-121 ± 37	-831 ± 37	1642 ± 53	-0.38 ± 0.03
3C 273	...	-11.50 ± 0.05	1.00	637 ± 89	-2031 ± 89	7277 ± 125	0.00 ± 0.02	...	...	...	...
Mrk 231	...	-11.14 ± 0.04	0.62	-321 ± 20	-2421 ± 20	6396 ± 29	-0.29 ± 0.00	...	...	...	...
F13218	0.73 ± 0.07	-10.09 ± 0.04	0.80	-400 ± 18	-1730 ± 18	2924 ± 25	-0.76 ± 0.01	-1064 ± 69	-1755 ± 69	2140 ± 98	-0.98 ± 0.06
F13305	1.18 ± 0.12	-13.45 ± 0.04	1.01	17 ± 97	-371 ± 97	1066 ± 137	0.15 ± 0.13	55 ± 127	-453 ± 127	1398 ± 180	0.14 ± 0.13
Mrk 273	1.94 ± 0.19	-12.70 ± 0.03	0.72	...	...	...	...	...	...	...	...
F14070	2.11 ± 0.21	-12.82 ± 0.04	1.22	...	...	...	...	...	...	...	...
F15001	1.04 ± 0.10	-14.00 ± 0.05	0.62	-54 ± 69	-330 ± 69	897 ± 98	-0.37 ± 0.12	-107 ± 69	-590 ± 69	1036 ± 98	-0.69 ± 0.11
F15250	0.62 ± 0.06	-14.60 ± 0.04	0.60	51 ± 69	-87 ± 69	552 ± 98	0.35 ± 0.19	67 ± 69	-71 ± 69	483 ± 98	0.32 ± 0.21
F16156	0.71 ± 0.07	-13.39 ± 0.03	0.75	123 ± 112	-439 ± 113	1909 ± 159	0.19 ± 0.08	-54 ± 147	-644 ± 148	1474 ± 208	-0.27 ± 0.15
F21219	...	-12.17 ± 0.04	0.73	11 ± 4285	-788 ± 5083	2627 ± 6278	0.20 ± 2.44	-490 ± 131	-1147 ± 132	3015 ± 185	0.20 ± 0.06
F23060	1.15 ± 0.11	-12.03 ± 0.03	1.04	133 ± 69	-419 ± 69	2071 ± 98	0.13 ± 0.05	12 ± 69	-403 ± 69	1104 ± 98	-0.35 ± 0.09
F23233	0.59 ± 0.06	-14.70 ± 0.05	1.02	70 ± 69	-344 ± 69	828 ± 98	-0.32 ± 0.12	-189 ± 69	-673 ± 69	1381 ± 98	-0.57 ± 0.08

Note. Column (2): Color excess based on the Balmer decrement measured from the optical spectra described in Section 2.3.3. Column (3): Extinction-corrected Hα flux in logarithm and cgs units. Column (4): Aperture correction factor applied to the Hα flux in the calculation of $f_{\mathrm{esc}}(\mathrm{Ly}\alpha)$. Columns (5)–(8): Kinematic properties v_{50}, v_{80}, W_{80}, and A_{91} of Hα emission. Column (9)–(12): Kinematic properties v_{50}, v_{80}, W_{80}, and A_{91} of [O III] λ5007 emission.

Table 5
Properties of the O VI and N V Absorption Features

Name	W_{eq} (Å)	v_{wtavg} (km s^{-1})	σ_{rms} (km s^{-1})	log($N_{ion,\ d}$) (cm^{-2})	$C_{f,\ d}$	# comp.	log(N_{ion}) (cm^{-2})	C_f
(1)	(2)	(3)	(4)	(5)	(6)	(7)	(8)	(9)
F01004, O VI	10.59 ± 0.26	-2720 ± 110	1470 ± 120	...	...	1	>17.1	...
F01004, N V	<0.14	...	...	...	...	...	...	...
Mrk 1014, O VI	<0.09	...	...	...	...	...	...	...
Mrk 1014, N V	<0.13	...	...	...	...	...	...	...
F05189, N V	<0.07	...	...	...	...	...	...	...
F07599, N V	55.39 ± 0.07	-12690 ± 20	4620 ± 10	...	...	1	>17.2	...
Z11598, O VI	2.03 ± 0.12	-190 ± 30	90 ± 40	**>16.4**	0.80 ± 0.05	2	**>16.3**, 14.5 ± 0.3,	0.90 ± 0.03, 1(f)
Z11598, N V	2.07 ± 0.12	-170 ± 30	100 ± 30	**>16.1**	0.57 ± 0.22	1	**>15.9**	0.82 ± 0.03
3C 273, O VI	<0.04	...	...	...	...	...	...	...
3C 273, N V	<0.04	...	...	...	...	...	...	...
Mrk 231 N V	<0.18	...	...	...	...	...	...	...
F13218, O VI	2.23 ± 0.18	-250 ± 40	150 ± 50	**>15.6**	0.66 ± 0.12	3	**>15.7**, **>15.2**, **>15.9**	0.79 ± 0.05, 0.79 ± 0.09, 0.55 ± 0.04
F13305, N V	<0.07	...	...	...	...	...	...	
F21219, O VI	1.17 ± 0.05	-4400 ± 190	180 ± 20	...	...	4	14.1 ± 0.2, 14.5 ± 0.2, 14.2 ± 0.1, 14.2 ± 0.1	1(f), 1(f), 1(f), 1(f)
F21219, N V	1.28 ± 0.05	-4430 ± 300	190 ± 30	14.8 ± 0.2	0.78 ± 0.20	4	14.4 ± 0.1, 13.6 ± 0.1, 14.2 ± 0.1, 13.5 ± 0.1	1(f), 1(f),1(f), 1(f)
F23060, N V	1.34 ± 0.24	-610 ± 150	160 ± 130	...	...	2	14.2 ± 1.6, 14.1 ± 1.6	1(f), 1(f)

Note. Column (1): Object and absorption feature name. Columns (2)–(4): Velocity-integrated EW, W_{eq}(Equation (5)), average depth-weighted velocity v_{wtavg} (Equation (6)), and average depth-weighted velocity dispersion σ_{rms} (Equation (7)) of the absorption lines. Column (5): Ion column densities obtained from the analysis of the absorption doublet with partial covering model as described in Section 3.3.1. Column (6): Velocity-weighted covering fractions calculated from the same analysis for ion column densities in Column (5). Column (7): Number of components in the best fits from the Voigt profile fits as described in Section 3.3.2. Notice that the O VI absorption in F01004 and the N V absorption of F07599 are BAL, and the one-component fit is only tentative/experimental, with the aim of capturing the overall absorption profile. Column (8): Ion column densities from the Voigt profile fits. The values for individual components from the best-fit model are separated by commas. This is also true for Column (9). Column (9): Covering fractions from the Voigt profile fits. The flag "f" in parenthesis indicates that the covering fraction is fixed to the corresponding value in the fits.

and the weighted outflow velocity dispersion,

$$\sigma_{wtavg} = \left\{ \frac{\int (v - v_{wtavg})^2 [1 - f(v)] dv}{W_{eq}} \right\}^{\frac{1}{2}}. \quad (7)$$

The results are summarized in Table 5.

3.3.1. Evidence of Partial Covering for the O VI and N V Doublets

The profiles of the resolved O VI and N V doublets may be used to derive the basic characteristics of the absorbing cloud—background source system. For the absorption features in Z11598 and F13218, there is evidence of partial covering: the optical depth ratio of the spectrally resolved doublet deviates from the theoretical expectation from a simple model where the foreground cloud is illuminated by the background point source with a 100% covering fraction.

For the cases where the optical depths of the doublets (proportional to λf_{osc}, the product of wavelength and oscillator strength) differ by a factor of ~2 (like O VI 1032, 1038 and N V 1238, 1243), and the continuum intensity is normalized to unity, the coverage fraction (or covering factor, C_f) as a function of velocity may be obtained. Following Hamann et al. (1997a), in the simple situation where the two transitions of the doublet do not overlap with each other, we have

$$C_f(v) = \frac{I_1(v)^2 - 2I_1(v) + 1}{I_2(v) - 2I_1(v) + 1}; \quad I_1 > I_2 \geqslant I_1^2 \quad (8)$$

$$C_f(v) = 1; \quad I_2 < I_1^2 \quad (9)$$

$$C_f(v) = 1 - I_1(v); \quad I_2 \geqslant I_1. \quad (10)$$

Here, I_1 and I_2 are the normalized intensities of the weaker and stronger absorption lines, respectively, and C_f is the covering factor.

Then the optical depth as a function of the velocity can be written as

$$\tau_1(v) = ln\left(\frac{C_f(v)}{I_1(v) + C_f(v) - 1}\right) \quad (11)$$

$$\tau_2(v) = 2\tau_1(v). \quad (12)$$

The column density of the ion can then be obtained by integrating the optical depth over the velocity and adopting

$$N_{ion} = \frac{m_e c}{\pi e^2 f \lambda} \int \tau(v) dv. \quad (13)$$

The resulting values of N_{ion} are listed in Table 5.

3.3.2. Voigt Profile Fitting of O VI and N V Absorbers

A popular approach to quantify the absorption features is to fit them with the product of individual components, assuming Voigt profiles for the optical depth distribution in frequency (or velocity, wavelength) space. As discussed in Section 3.3.1, there is evidence for partial covering in a few objects. To account for this, we also include a constant covering fraction parameter for each component of the model. The final model of the normalized intensity can then be written as

$$I(\nu) = \prod \{1 - C_f[1 - e^{-\tau(\nu)}]\} \quad (14)$$

$$\tau(\nu|N, b, z) = N\sigma_0 f_{\rm osc}\Phi(\nu|b, z), \quad (15)$$

where C_f, τ, ν, N, b, $f_{\rm osc}$, and σ_0 are the covering fraction parameter, optical depth, frequency, ion column density, Doppler parameter, oscillator strength, and cross section, respectively. $\Phi(\nu|b, z)$ is the normalized Voigt profile. The adopted atomic parameters are taken from Morton (2003).

In the fitting procedures, the model described above is further convolved with the line-spread function of HST/COS tabulated on the HST/COS website.[8] We adopt a customized software built on the nonlinear least-squares fit implemented in LMFIT to search for the best-fit model. In our software, a velocity component is added to the model if the Bayesian Information Criterion (BIC; Ivezić et al. 2019) decreases, and this process stops when the minimum BIC value is found. The model with the lowest BIC value is then chosen as the best fit to the data, which is also confirmed by a visual inspection. In addition, we have tested this by manually fitting the absorption line profile with n+1 components when n components are required by the best fit. The change in total column density is in general $\lesssim$0.1 (in logarithm), within the uncertainty of total column density derived from the best-fit model. The uncertainties of the best-fit parameters are calculated from the 1σ (68.3%) confidence interval, adopting the conf_interval function of LMFIT, which takes into account the covariances between blended absorption components.

The best fits for all absorbers clearly detected in our sample are shown in Figure 6. The covering factor, C_f, is fixed to unity in two objects: for F21219, the fit is unable to break the degeneracy between the covering factor and ion column density; and for F23060, no evidence of partial covering is suggested by the data. For Z11598 and F13218, the ion column densities are reported as lower limits due to the saturation of the absorption features. Additionally, the fits for the N V BAL in F07599 and O VI BAL in F01004 are highly uncertain, given the model parameter degeneracy caused by the saturation and smoothness of the absorption feature, as well as the large uncertainties in the continuum determination.

Following Paper I, our fitting scheme assumes that the velocity dependence of the optical depth can be parameterized as the sum of discrete independent components with Voigt profiles and constant covering fractions, and that the individual absorbers simply overlap with each other along the line of sight. In reality, the C_f is probably a more complex function of velocities (Arav et al. 2005, 2008, 2013), and the absorbing materials may completely overlap, partially overlap, or not overlap each other. While our approach cannot account for these details, it is sufficient to meet our primary goal, which is to characterize the overall strength and kinematics of these absorbers, and to put constraints on the ion column density.

The column densities and covering fractions from these fits are summarized in Table 5. For sources Z11598, F13218, and F21219, the results are consistent with those obtained from the analysis of the absorption doublets with partial covering model as described in Section 3.3.1. Further discussion based on these fits is postponed until Section 5.

[8] https://www.stsci.edu/hst/instrumentation/cos/performance/spectral-resolution

4. Origin of the Lyα Emission

Intuitively, strong Lyα emission is not expected in dusty ULIRGs, due to the huge optical depth. The origin of Lyα emission in our objects is therefore worth investigating. In this section, we focus on three factors that may help with the production and/or escape of Lyα photons in our ULIRG sample:

(i) AGN: The AGN activity may intrinsically produce more Lyα photons than what we have assumed. For example, the gas density may be so high in the broad line region (and perhaps also the narrow line region) of an AGN that collisional excitation becomes important in promoting Lyα emission (e.g., Dijkstra 2017). Radiation from the AGN may also ionize the gas and destroy the dust in the Lyα-emitting regions and material along the line of sight, and therefore reduce the overall opacity to the Lyα emission. (ii) Outflow: The blueshifted Lyα emission may come from the outflowing gas. The velocity offset between the outflow and the interstellar medium decreases the optical depth to the Lyα emission radiated from the fast-moving gas. The outflow can also create low-opacity pathways for Lyα photons by clearing out the gas and dust. In addition, the outflow may have broken out of the dusty ISM, allowing the Lyα photons to escape freely. (iii) Dust: The Lyα photons are heavily affected by complicated, dust-related radiative transfer effects, which directly affect the observed properties of the Lyα emission in ULIRGs.

In our analyses, we adopt Kendall tau correlation tests to examine potential correlations between the properties of Lyα emission and those of the AGN, outflows, and dust reddening. Specifically, we adopt the method from Isobe et al. (1986) to compute the Kendall tau correlation coefficient. The p-value of the null hypothesis (no correlation) is calculated to show the statistical significance of the correlation. This method can handle censored data, which is the case for $\rm EW_{Ly\alpha}$ and $f_{\rm esc}$(Lyα). We use the implementation of pymccorrelation (Privon et al. 2020), which perturbs the data with a Monte Carlo method to compute the error in the correlation coefficient (Curran 2014). To expand the dynamic ranges of the variables in the analyses, by default, we also include the results of the starburst-dominated ULIRGs from M15, whenever possible. The results from these correlation tests are summarized in Table 6.

4.1. Effect of the AGN

First, we examine the possible link between the strength of the AGN (more specifically, the AGN luminosities, $L_{\rm AGN}$, and AGN fractions, $f_{\rm AGN}$; see Table 1) and the properties of Lyα emission. As shown in Figure 7, the EWs of Lyα ($\rm EW_{Ly\alpha}$) increase with both $L_{\rm AGN}$ and $f_{\rm AGN}$. The p-values are $\sim$0.002 and $\sim$0.023, based on the Kendall tau tests, respectively. In addition, $L_{\rm AGN}$ may also correlate with the kinematic properties

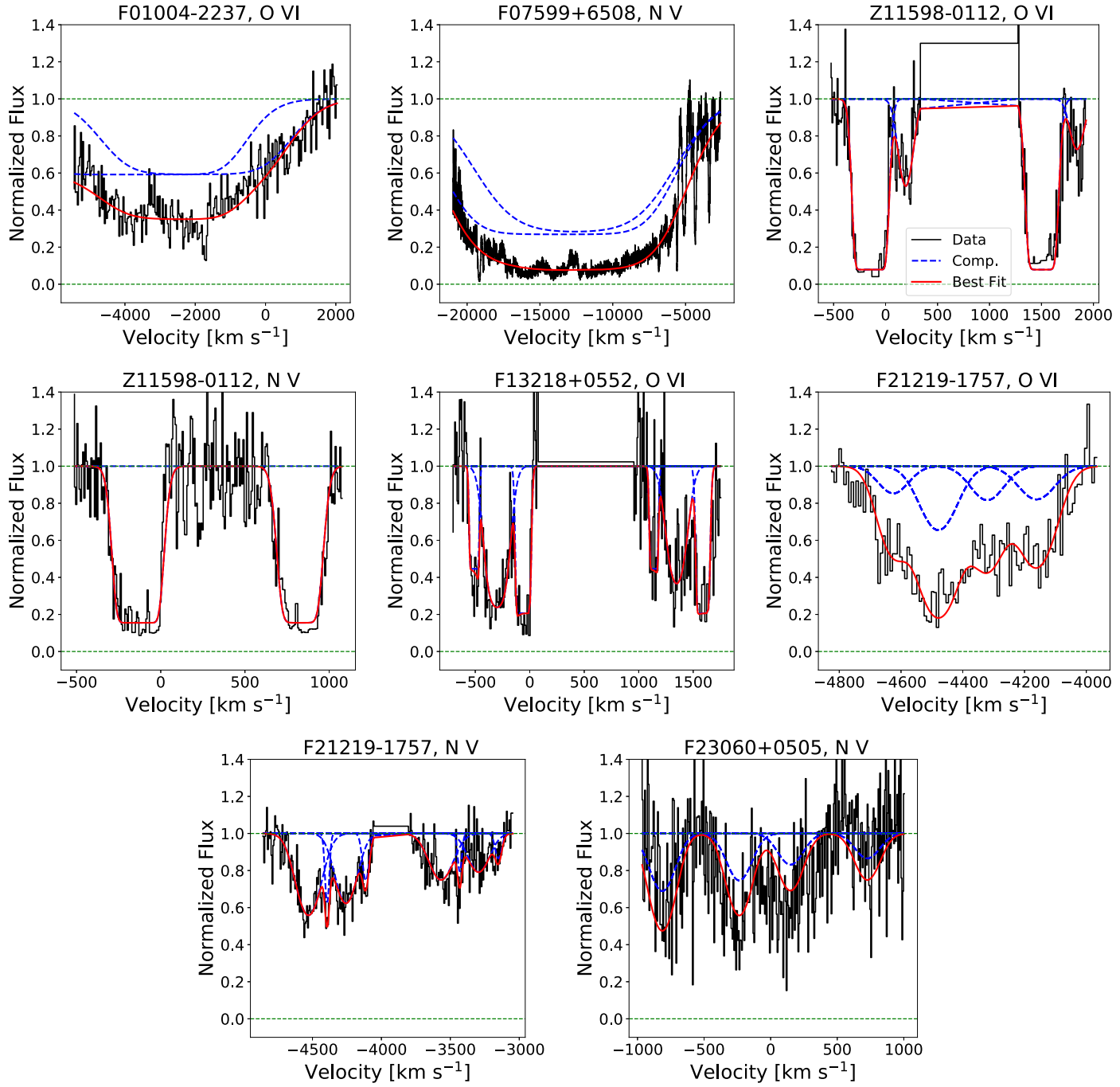

Figure 6. Best fits to the O VI 1032, 1038 and N V 1238, 1243 absorption features detected in our sample of ULIRGs using multicomponent Voigt profile fitting. Notice that, for the BAL in F01004 and F07599, the single-component fits are tentative/experimental, only aiming to capture the overall shape of the BAL. In each panel, the normalized flux density is shown by the black solid curve. The overall best-fit model and individual components of this model are shown by the red solid curve and blue dashed curves, respectively. All spectra are normalized to the local continuum and shown in the rest frame of the bluer transitions of corresponding objects.

of Lyα (v_{80}, v_{50}, A_{91}, and W_{80} of Lyα; p-values $\simeq$0.06–0.10). As an example, v_{80} of Lyα are plotted against $L_{\rm AGN}$ and $f_{\rm AGN}$ in Figure 8. These weak trends are mainly driven by the Type 1 sources with small v_{80} and large W_{80}; indeed, the correlations are not statistically significant (p-values $>$0.1) when the Type 1 sources are excluded.

Next, we explore the behavior of the Lyα escape fraction, $f_{\rm esc}$(Lyα), with the strength of the AGN, as shown in Figure 9. There are possible positive correlations between $L_{\rm AGN}$ and $f_{\rm esc}$(Lyα) (p-value $\simeq$0.062), and between $f_{\rm AGN}$ and $f_{\rm esc}$(Lyα) (p-value $\simeq$0.068). However, we note that these correlations are no longer significant (p-values $\simeq$0.2 and 0.4, respectively) if we exclude the data points of the starburst-dominated ULIRGs from M15.

4.2. Effect of the Outflow

The prevalence of blueshifted Lyα emission-line profiles in our sample, as stated in Section 3.1, hints at a potential link between outflows and the Lyα emission in our objects.

Table 6
Correlation Tests with the Lyα Properties

x (1)	y (2)	Sample (3)	N (4)	p-value (5)	r (6)
L_{AGN}	$EW_{Ly\alpha}$	A	20	0.002	$0.49^{+0.13}_{-0.14}$
L_{AGN}	$f_{esc}(Ly\alpha)$	A	26	0.062	$0.26^{+0.16}_{-0.16}$
L_{AGN}	v_{80}	A	14	0.058	$-0.38^{+0.17}_{-0.15}$
L_{AGN}	v_{50}	A	14	0.095	$-0.34^{+0.18}_{-0.15}$
L_{AGN}	W_{80}	A	14	0.066	$0.37^{+0.18}_{-0.18}$
f_{AGN}	$EW_{Ly\alpha}$	A	20	0.023	$0.37^{+0.13}_{-0.14}$
f_{AGN}	$f_{esc}(Ly\alpha)$	A	26	0.068	$0.25^{+0.14}_{-0.14}$
f_{AGN}	v_{80}	A	14	0.470	$-0.08^{+0.19}_{-0.20}$
f_{AGN}	v_{50}	A	14	0.429	$-0.08^{+0.22}_{-0.21}$
f_{AGN}	W_{80}	A	14	0.439	$-0.08^{+0.20}_{-0.22}$
$v_{80,[O\ III]}$	$EW_{Ly\alpha}$	A	18	0.064	$-0.32^{+0.19}_{-0.16}$
$v_{80,[O\ III]}$	$f_{esc}(Ly\alpha)$	A	20	0.049	$-0.32^{+0.20}_{-0.16}$
$v_{80,[O\ III]}$	v_{80}	A	18	<0.001	$0.72^{+0.08}_{-0.11}$
$v_{80,[O\ III]}$	v_{80}	B	12	0.003	$0.65^{+0.14}_{-0.20}$
$v_{80,[O\ III]}$	v_{80}	C	8	0.008	$0.77^{+0.13}_{-0.23}$
$v_{50,[O\ III]}$	$EW_{Ly\alpha}$	B	12	0.398	$-0.06^{+0.30}_{-0.24}$
$v_{50,[O\ III]}$	$f_{esc}(Ly\alpha)$	B	13	0.381	$0.04^{+0.26}_{-0.26}$
$v_{50,[O\ III]}$	v_{50}	B	12	0.041	$0.45^{+0.18}_{-0.21}$
$v_{50,[O\ III]}$	v_{50}	C	8	0.013	$0.72^{+0.15}_{-0.26}$
$W_{80,[O\ III]}$	$EW_{Ly\alpha}$	B	12	0.439	$-0.05^{+0.25}_{-0.25}$
$W_{80,[O\ III]}$	$f_{esc}(Ly\alpha)$	B	14	0.228	$0.23^{+0.19}_{-0.22}$
$W_{80,[O\ III]}$	W_{80}	B	12	0.007	$0.60^{+0.14}_{-0.18}$
$W_{80,[O\ III]}$	W_{80}	C	8	0.083	$0.49^{+0.27}_{-0.27}$
$A_{91,[O\ III]}$	$EW_{Ly\alpha}$	B	12	0.285	$-0.20^{+0.28}_{-0.24}$
$A_{91,[O\ III]}$	$f_{esc}(Ly\alpha)$	B	14	0.468	$0.10^{+0.16}_{-0.18}$
$A_{91,[O\ III]}$	A_{91}	B	12	0.012	$0.56^{+0.13}_{-0.17}$
$A_{91,[O\ III]}$	A_{91}	C	8	0.017	$0.69^{+0.17}_{-0.20}$
$v_{80,H\alpha}$	$EW_{Ly\alpha}$	B	14	0.174	$-0.26^{+0.29}_{-0.23}$
$v_{80,H\alpha}$	$f_{esc}(Ly\alpha)$	B	17	0.428	$-0.06^{+0.20}_{-0.20}$
$v_{80,H\alpha}$	v_{80}	B	14	0.001	$0.64^{+0.10}_{-0.13}$
$v_{50,H\alpha}$	$EW_{Ly\alpha}$	B	14	0.534	$-0.03^{+0.19}_{-0.18}$
$v_{50,H\alpha}$	$f_{esc}(Ly\alpha)$	B	15	0.316	$0.13^{+0.20}_{-0.26}$
$v_{50,H\alpha}$	v_{50}	B	14	0.437	$0.01^{+0.22}_{-0.24}$
$W_{80,H\alpha}$	$EW_{Ly\alpha}$	B	14	0.203	$0.23^{+0.21}_{-0.28}$
$W_{80,H\alpha}$	$f_{esc}(Ly\alpha)$	B	16	0.411	$-0.03^{+0.23}_{-0.21}$
$W_{80,H\alpha}$	W_{80}	B	14	0.005	$0.56^{+0.13}_{-0.14}$
$A_{91,H\alpha}$	$EW_{Ly\alpha}$	B	14	0.373	$0.00^{+0.27}_{-0.26}$
$A_{91,H\alpha}$	$f_{esc}(Ly\alpha)$	B	16	0.466	$-0.10^{+0.18}_{-0.16}$
$A_{91,H\alpha}$	A_{91}	B	14	0.039	$0.41^{+0.16}_{-0.20}$
$E(B-V)$	$f_{esc}(Ly\alpha)$	A	20	0.371	$0.00^{+0.20}_{-0.22}$

Note. Column (1): Independent variable (AGN and host galaxy property). Column (2): Dependent variable (Lyα property). Column (3): Flag for the sample adopted in the analysis. A: Our ULIRG sample + the ULIRG sample from M15. B: Our ULIRG sample alone. C: Sources with Type 2 AGN in our ULIRG sample. Column (4): Number of data points. Column (5): p-value of null hypothesis (no correlation) from the Kendall tau correlation test. Column (6): Kendall tau correlation coefficient r with the associated 1σ error.

Therefore, we start by simply checking whether there is a correlation between the $EW_{Ly\alpha}$ and v_{80} of Lyα, and confirm a positive result (p-value $\simeq$0.02). However, we note that this trend disappears (p-values >0.1) if we do not include the starburst-dominated objects from M15. Similarly, we have also checked the potential correlation between $f_{esc}(Ly\alpha)$ and v_{80} of Lyα, but no statistically significant trend is present (p-value $\simeq$0.13).

4.2.1. Connection with the Ionized Outflow in Emission

The blueshift of the nonresonant, forbidden emission [O III] λ5007 line in galaxies is strong evidence for ionized gas outflows (Veilleux et al. 2005). To investigate the connection between the blueshift of the Lyα emission and [O III] outflowing gas, it is thus natural to determine whether the kinematic properties derived from the Lyα emission line are correlated with those based on the [O III] λ5007 emission. This comparison is shown in Figure 10.

The most significant trend observed in our sample is the positive correlation between v_{80} of Lyα and [O III] λ5007, with p-value <0.001. This trend still holds if the data from M15 are excluded (p-values $\simeq$0.003), or if only the type 2 sources are considered in the analysis (p-value $\simeq$0.008). The values of v_{50}, W_{80}, and A_{91} of Lyα also show positive correlations with those of [O III] λ5007, although they are statistically less significant (p-values of $\sim$0.007–0.041 from the Kendall tau tests[9]; see Table 6).

Additionally, as shown in Figure 11, there may be weak correlations between $v_{80,[O\ III]}$ (notice that this quantity is negative in the case of outflows) and $EW_{Ly\alpha}$ (p-value $\simeq$0.064), and between $v_{80,[O\ III]}$ and $f_{esc}(Ly\alpha)$ (p-value $\simeq$0.049). This suggests that, to some extent, outflows may help clear the path for Lyα photons to escape. However, these weak trends are no longer significant when the objects from M15 are excluded. Moreover, no statistically significant trends are visible when considering the other kinematic properties of [O III] λ5007 ($v_{50,[O\ III]}$, $W_{80,[O\ III]}$, and $A_{91,[O\ III]}$).

For the sake of completeness, we also briefly discuss the strong Hα line emission in these objects. We note that v_{80}, W_{80}, and A_{91} of Hα are positively correlated with those of Lyα (p-value $\simeq$0.001–0.039; see Table 6), whereas no correlation is seen between v_{50} of Hα and Lyα (p-value $\simeq$0.437). While blueshifted Hα emission may indicate outflowing gas, Hα is likely dominated by the emission from the broad emission line region (BELR) in Type 1 sources (e.g., 3C 273, Mrk 1014; see Figure 5). In addition, the nearby [N II] $\lambda\lambda$6548, 6583 emission lines add uncertainty to the kinematic measurements based on Hα. Therefore, we do not use the Hα-based kinematics to examine the link between the blueshifts of Lyα and the ionized outflows in the remainder of the paper.

4.2.2. Connection with the O VI and/or N V Outflows

As discussed in Section 3.3, highly ionized O VI and/or N V outflows are detected in the HST/COS spectra of our ULIRGs. Among the nine objects with both Lyα measurements and continuum S/N high enough to allow for relatively solid detection of O VI and/or N V absorption features, four of them show O VI and/or N V outflows. There is no clear difference in the mean values and overall ranges of the Lyα escape fractions between the objects with and without O VI and/or N V outflows. The mean value of the Lyα EWs in the objects without outflow detection in O VI and/or NV is higher than those with outflows by $\sim$60%. However, these results are based on a very small sample, so no statistically robust conclusion may be drawn.

[9] As a reminder, in the analyses including $v_{50,[O\ III]}$, $W_{80,[O\ III]}$, and $A_{91,[O\ III]}$, we do not consider the sources from M15, as the corresponding measurements are not publicly available.

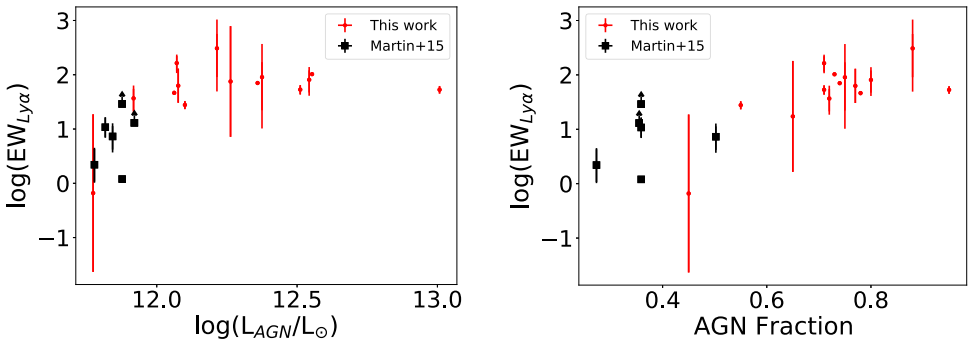

Figure 7. The Lyα EWs for the ULIRGs in our sample (red) and those from M15 (black) vs. AGN luminosities (left) and AGN fractions (right). There are statistically significant positive correlations between $L_{\rm AGN}$ and EW$_{\rm Ly\alpha}$, and between $f_{\rm AGN}$ and EW$_{\rm Ly\alpha}$.

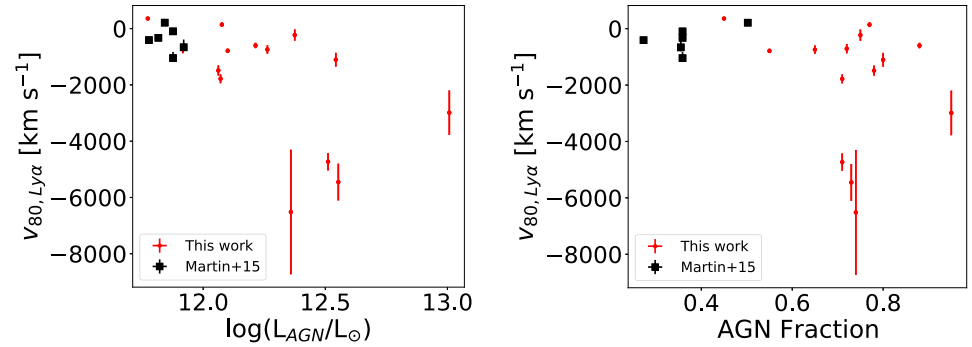

Figure 8. The 80th percentile velocities v_{80} of Lyα for the ULIRGs in our sample (red) and those from M15 (black) vs. AGN luminosities (left) and AGN fractions (right). There are weak correlations between $L_{\rm AGN}$ and v_{80}, and between $f_{\rm AGN}$ and v_{80}, which are, however, mainly driven by the Type 1 sources with small v_{80}.

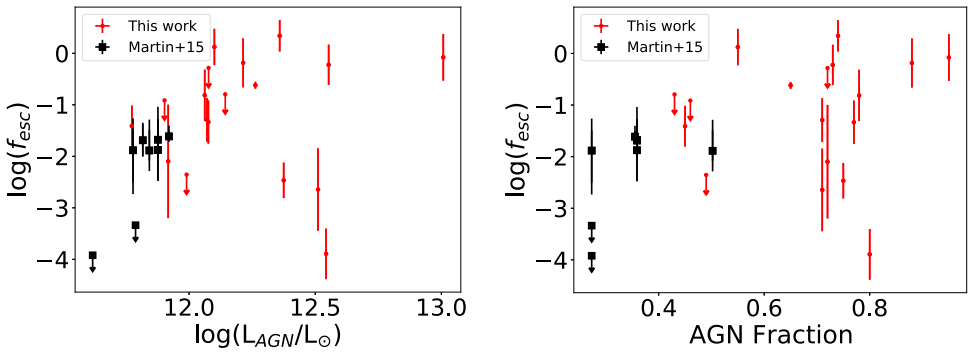

Figure 9. The Lyα escape fractions for the ULIRGs in our sample (red) and those from M15 (black) vs. AGN luminosities (left) and AGN fractions (right). There may be weak correlations between $L_{\rm AGN}$ and $f_{\rm esc}$(Lyα), and between $f_{\rm AGN}$ and $f_{\rm esc}$(Lyα), when both the data from our sample and sources in Martin+15 are considered.

4.2.3. Connection with the Neutral Phase Outflows

Neutral gas outflows, traced by the blueshifted Na I D $\lambda\lambda$5890, 5896 absorption features, are often detected in ULIRGs (e.g., Rupke et al. 2005; Rupke & Veilleux 2011, 2013b; Rupke et al. 2017). As shown in Figure 12, three of our objects have both blueshifted Lyα emission and blueshifted interstellar Na I D absorption features with similar kinematics. Specifically, for F05189, v_{50} of Lyα emission is similar to that of the blueshifted component of the Na I D absorption ($\sim$−400 km s^{-1}). For F11119, the blueshifted peak of the Lyα emission and the v_{50} of the Na I D absorption have similar velocities of $\sim$−800 km s^{-1}. For Mrk 231, the v_{50} of the Na I D absorption ($\sim$−5000 km s^{-1}) is close to the velocity of the peak of the blueshifted wing of Lyα emission. Overall, if the blueshifted Lyα emission is indeed tracing the outflowing gas, as argued in Section 4.2.1, the results above hint at a possible connection between the outflowing gas traced by blueshifted Lyα and the outflowing neutral gas in these three objects. For instance, Lyα could be scattered off of the outflowing neutral gas traced by Na I D. However, given the very small number of objects where the Lyα−Na I D comparison was possible, these results may not apply to all objects in the sample.

4.3. Effect of Dust

Complex dust-related radiative transfer processes may shape the observed Lyα emission. In the following, we explore how dust and its distribution within the galaxy may affect the escape of Lyα photons qualitatively, by examining the relation between the nebular line color excess, $E(B-V)$ (reflecting dust reddening of the line-emitting gas) and $f_{\rm esc}$(Lyα). A more quantitative analysis of this issue requires a careful modeling of

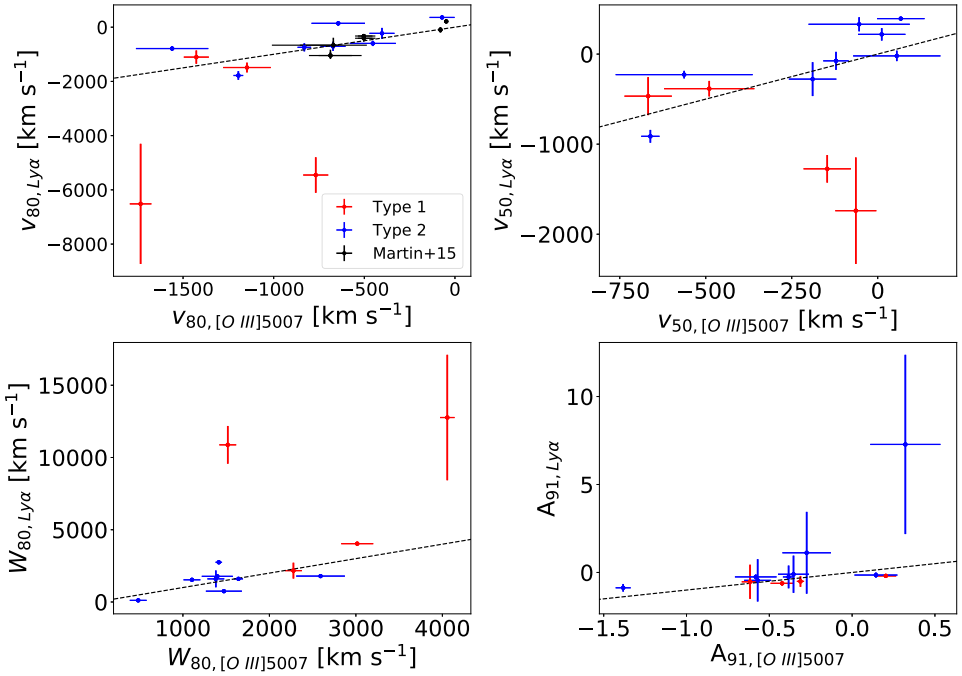

Figure 10. Comparisons of the kinematic properties derived from Lyα and [O III] λ5007. From top left to bottom right, v_{80}, v_{50}, W_{80}, and A_{91} are shown. The ULIRGs with Type 1 and Type 2 AGN in our sample are shown in red and blue, respectively. In the upper left panel, the ULIRGs from M15 are shown in black. The black dashed lines indicate the 1:1 equality lines. The v_{80} of Lyα and [O III] λ5007 emission lines correlate with each other. Other kinematic properties of the Lyα and [O III] λ5007 emission lines are also correlated, but less significantly.

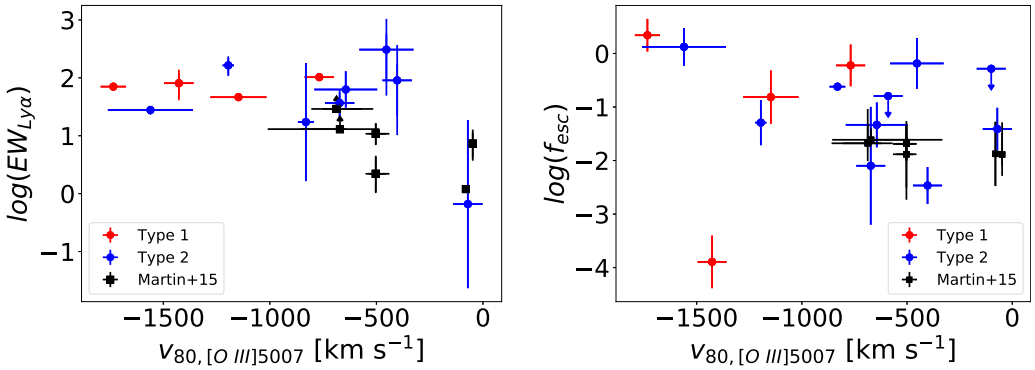

Figure 11. The Lyα EWs (left) and Lyα escape fractions (right) for the Type 1 (red) and Type 2 (blue) ULIRGs in our sample and the starburst-dominated ULIRGs from M15 (black) as functions of the 80th percentile velocities v_{80} of [O III] λ5007 emission lines. There are weak correlations between $v_{80,[O\ III]}$ and $EW_{Ly\alpha}$, and between $v_{80,[O\ III]}$ and f_{esc}(Lyα), when both the data from our sample and sources in Martin+15 are considered.

the radiative transfer processes, which is beyond the scope of this paper.

In Figure 13, we plot f_{esc}(Lyα) as a function of $E(B-V)$ for both our objects and the starburst-dominated ULIRGs from M15. Also shown in the figure is the expected f_{esc}(Lyα) given the continuum attenuation at the Lyα transition derived from the values of $E(B-V)$ based on the Cardelli et al. (1989) reddening curve. In the figure, there is a lack of correlation between the $E(B-V)$ and f_{esc}(Lyα) (p-value $\simeq$0.371 from the Kendall tau test; see Table 6), which is inconsistent with the naive expectation that f_{esc}(Lyα) should decrease with increasing $E(B-V)$. In addition, the Lyα emissions in 6 out of the 14 ULIRGs with clear Lyα detections show f_{esc}(Lyα) much higher than the values expected from the reddening curve. Similar phenomena have been seen in nearby Lyα-emitting galaxies with $E(B-V) \gtrsim 0.3$, where Lyα emission is on average several times stronger than expected (Scarlata et al. 2009; Atek et al. 2014; Hayes et al. 2014).

The two phenomena described above may be caused by the fact that our observations reflect the integrated properties of regions with various dust extinction within one galaxy. The observed emission lines come from both the dusty regions (more likely located in the central parts of the systems) and dust-free/less dusty regions such as broad line region of the AGN, off-nuclear H II region, diffused ionized gas, gas that is tidally stripped during the merging process, or even outflowing gas at a large distance from the nucleus. The observed Lyα flux and $E(B-V)$ are the integrated values of all these regions with different weights, which may therefore lead to large scatters in the relation between $E(B-V)$ and f_{esc}(Lyα). The higher f_{esc}(Lyα) at a given $E(B-V)$ may be explained if dusty regions bias the overall $E(B-V)$ to a value higher than those

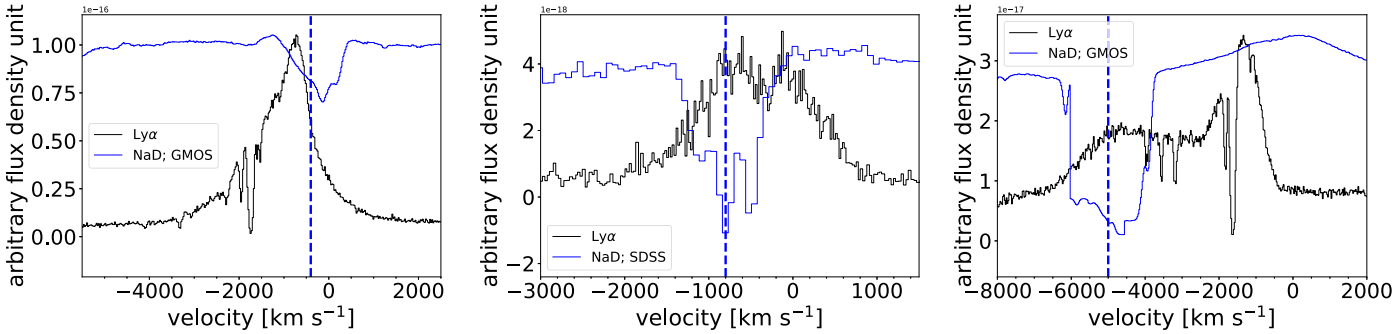

Figure 12. Comparison between the Lyα (black) and Na I D $\lambda\lambda$5890, 5896 (blue) profiles for sources F05189 (left), F11119 (middle), and Mrk 231 (right). The blue dashed lines indicate the v_{50} of the outflowing Na I D $\lambda\lambda$5890, 5896 component from Rupke et al. (2005), excluding the systemic component in F05189. The spectra are scaled for display purposes, and the y-axes are in arbitrary flux density units.

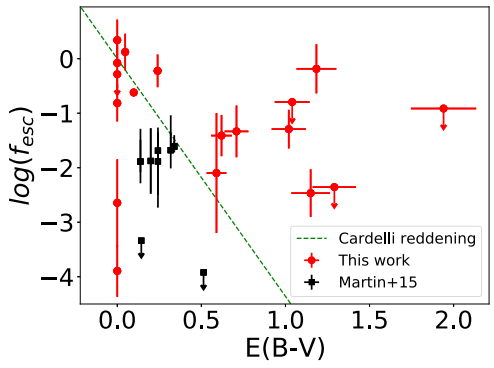

Figure 13. Lyα escape fractions, f_{esc}(Lyα), for the AGN-dominated ULIRGs in our sample (red: Type 1 AGN; blue: Type 2 AGN) and the starburst-dominated ULIRGs from M15 (black) as a function of the color excess $E(B-V)$. The green dashed line indicates the continuum attenuation at the wavelength of Lyα transition as given by a Cardelli et al. (1989) reddening curve and the color excess (measured from the Balmer decrement).

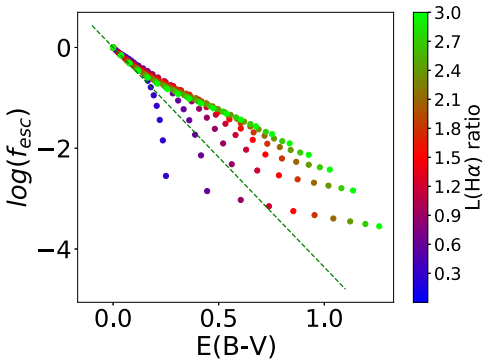

Figure 14. f_{esc}(Lyα) as a function of $E(B-V)$ from a simple model reflecting the effect of mixing two ionized gas clouds: one cloud with no dust content and Hα luminosity of unity, and the other one with increasing dust reddening and Hα luminosity. The Hα luminosity ratio of the dusty cloud to the dust-free cloud is indicated by the color of the data point. Along each track of data points with the same color, the $E(B-V)$ of the dusty cloud increases from left to right. The green dashed line indicates the same continuum attenuation as shown in Figure 13.

of less dusty regions where most of the observed Lyα emission comes from (this scenario has been pointed out in previous work; e.g., Atek et al. 2014). To illustrate this point, we build a simple model that considers the total Lyα and Balmer emission lines from two ionized gas clouds: one with zero dust reddening, and one with increasing dust reddening. The Hα luminosity ratios of the two regions are also varied. The overall $E(B-V)$ and f_{esc}(Lyα) integrated over the two gas clouds are shown in Figure 14. At large $E(B-V)$, the f_{esc}(Lyα) can be easily larger than the expected values based on the dust extinction curve, adopting Case B. In addition, the overall distribution of the data points can also mimic the scatter/noncorrelation seen in Figure 13.

Similarly, the enhancement of f_{esc}(Lyα) may also be caused by the internal geometry of the ISM and the dust distribution within it that, together, change the behavior of Lyα photons with respect to dust attenuation. At least two possible solutions have been proposed by previous works: (i) Atek et al. (2009) and Finkelstein et al. (2009) have invoked the Neufeld (1991) geometry where dust is embedded within the H I clumps of a multiphase ISM, and the scattering of Lyα photons prevents them from encountering dust. However, radiative transport simulations show that this effective "boost" of Lyα is very difficult unless parameters are carefully fine-tuned (Laursen et al. 2013; Duval et al. 2014). The predicted increase of Lyα EW with measured attenuation is not observed in our sample. (ii) Instead, Scarlata et al. (2009) argue for a scenario that is also built upon a clumpy dust distribution. It neither requires preservational scattering as in scenario (i) nor predicts that Lyα EW will increase with $E(B-V)$.

Alternatively, the higher-than-expected f_{esc}(Lyα) in the six sources may be caused by higher intrinsic Lyα emission. Such deviation from Case B may be caused by the high-density gas within the BELR of the AGN, where the collisional excitation enhances the intrinsic Lyα emission. Nevertheless, following this logic, it may be odd that the higher-than-expected f_{esc}(Lyα) are mostly seen in Type 2 sources rather than Type 1 sources where the Lyα enhancement due to the dense BELR should be more prominent. For example, in the Type 1 source 3C 273, while the broad Lyα emission line resembles the broad Hα emission line (see Figure 5) and is thus likely originated from the BELR, the f_{esc}(Lyα) in 3C 273 is close to the expected value under Case B conditions.

4.4. Overall Trends

In short, the analyses above indicate that the EWs of Lyα are more closely related to the strength of AGN activity (e.g., L_{AGN}, f_{AGN}), while the blueshifts of Lyα emission are more closely linked to those of nonresonant optical emission lines tracing ionized gas outflows. It is likely that the AGN activity governs the overall production of Lyα emission and the outflowing gas generates the blueshifted Lyα emission.

Additionally, the Lyα escape fractions, $f_{\rm esc}$(Lyα), tend to be slightly higher in sources with stronger AGN and faster outflows. Nevertheless, the $f_{\rm esc}$(Lyα) does not correlate with the dust reddening, $E(B-V)$, and 6 out of the 14 objects show $f_{\rm esc}$(Lyα) higher than the expectation from attenuation adopting Case B conditions and the extinction curve from Cardelli et al. (1989).

5. O VI and N V Absorbers in the ULIRGs

5.1. Origin of the O VI and N V Absorbers

We now turn our attention to the O VI and N V absorption features. Given the general blueshifts of these features, they are most likely tracing gas driven out of these galaxies by the starburst and/or AGN. Other possible origins include tidal debris from the galaxy merger, intervening circumgalactic medium (CGM), and stellar absorption.

Following Paper I, the characteristics of O VI and N V absorption features that indicate a quasar-driven wind origin include (1) line profiles that are broad and smooth compared to the thermal line widths (10–20 km s^{-1} for N^{4+} and O^{5+}) of ions at temperature $T \simeq 10^{4.5}$–$10^{5.5}$ K, (2) line ratios of the doublets O VI $\lambda1032/\lambda1038$ and N V $\lambda1238/\lambda1243$ that imply partial covering of the quasar emission source, and perhaps (3) large column densities in these high-ionization ions and/or high O VI/H I column density ratios (Hamann et al. 1997a, 1997b; Tripp et al. 2008; Hamann et al. 2019).

All blueshifted O VI and N V absorbers detected in the six ULIRGs meet criterion (1) except for the two narrow ($\sigma \sim 30$ km s^{-1}) components out of the three components in the best-fit O VI profile of F13218 and the two narrow ($\sigma \sim 20$–30 km s^{-1}) components out of the four components in the best-fit N V profile of F21219.[10] In addition, the O VI and N V absorption features in Z11598 and F13218 meet criterion (2), and the deep BAL features in F01004 and F07599 suggest potentially high column densities in agreement with criterion (3). So, in the end, all six ULIRGs show certain O VI and N V absorption features consistent with quasar-driven winds. This translates into an apparent outflow incidence rate of ~50%, close to that of the quasar sample in Paper I. We will expand on this topic in Section 6.

In contrast, the redshifted component of the O VI 1032, 1038 absorption feature in Z11598 may arise from tidal debris or infalling gas. It is not likely associated with the CGM, given that such relatively strong N V absorption line is rarely found in CGM studies at low redshift (Werk et al. 2016), albeit with several notable exceptions (Ding et al. 2003; Lehner et al. 2009; Savage et al. 2010; Tripp et al. 2011; Muzahid et al. 2015; Rosenwasser et al. 2018; Gatkine et al. 2019; Zahedy et al. 2020). In addition, we cannot rule out the possibility that the two narrow components ($|v| \lesssim 500$ km s^{-1}, $\sigma \sim 30$ km s^{-1}) in the O VI profile of F13218 come from the turbulent ISM and/or CGM of the system.

5.2. Location and Energetics of the Outflows

Here, we start with the constraints on the location of the O VI and N V absorbers detected in our ULIRG sample. In Z11598 and F13218 (and perhaps also all of the other four ULIRG with detected absorbers), the O VI and/or N V absorption features are deeper than the FUV continuum level, implying that part of the O VI and N V emission produced in the BELR is also absorbed. These absorbers are thus located outside the BELR, which has a scale of

$$r_{\rm BELR} \simeq 0.1 \left(\frac{\lambda L_\lambda (1350\text{Å})}{2 \times 10^{46}\ {\rm erg\ s^{-1}}} \right)^{0.55} {\rm pc} \quad (16)$$

(e.g., Kaspi et al. 2005, 2007; Bentz et al. 2013). The Equation (16) above is based on the C IV-traced BELR size–luminosity relation from Equation (2) in Kaspi et al. (2007), and the denominator, 2×10^{46} erg s^{-1}, corresponds to the $\lambda L_\lambda (1350\,\text{Å})$ of 3C 273. This typical scale is also consistent with the VLTI/GRAVITY result on the size of the BELR of 3C 273 ($r \simeq 0.12 \pm 0.03$ pc; Gravity Collaboration et al. 2018).

As for the upper limit on the radial distance of the outflows, qualitative constraints exist for the two objects with evidence of partial covering, Z11598 and F21219. The distance of the outflows in these two sources cannot be significantly larger than the size of the region where the continuum radiation comes from. The evidence of partial covering in these two objects also sets interesting limits on the size of the absorbing cloud: If the absorbing material is a single uniform cloud with a 100% filling factor, the cloud size should thus be $\lesssim$0.1 pc. However, if the absorbing material is made of multiple clouds, the partial covering may instead reflect the small filling factor of the clouds, and the sizes of individual clouds may be much smaller than 0.1 pc.

The mass, momentum, and kinetic energy outflow rates of the highly ionized outflow detected in our sample are estimated using the following equations:

$$\frac{dE}{dt} = 3.3 \times 10^{39} \left(\frac{Q}{0.15} \right) \left(\frac{N_H}{10^{22} {\rm cm^{-2}}} \right) \left(\frac{R}{0.1 {\rm pc}} \right) v_{1000}^3 \quad (17)$$

$$\frac{dp}{dt} = 6.7 \times 10^{32} \left(\frac{Q}{0.15} \right) \left(\frac{N_H}{10^{22} {\rm cm^{-2}}} \right) \left(\frac{R}{0.1 {\rm pc}} \right) v_{1000}^2 \quad (18)$$

$$\frac{dm}{dt} = 0.003 \left(\frac{Q}{0.15} \right) \left(\frac{N_H}{10^{22} {\rm cm^{-2}}} \right) \left(\frac{R}{0.1 {\rm pc}} \right) v_{1000}. \quad (19)$$

In the equations above, Q is an approximate global outflow covering factor quoted from Paper I, based on the incidence of mini-BALs in the SDSS quasars (Trump et al. 2006; Knigge et al. 2008; Gibson et al. 2009; Allen et al. 2011). Here, R is the radial distance of the outflow, with a value of 0.1 pc adopted as a placeholder for illustrative purposes; N_H is the column density of hydrogen; and v_{1000} is the outflow velocity in units of 1000 km s^{-1} obtained from the Voigt profile fits described in Section 3.3.2.

Note that the Voigt profile fits are highly uncertain for the O VI BAL in F01004, as well as the N V BAL in F07599, as stated in Section 3.3.2. Therefore, only rough estimations of the ion column densities may be obtained from the fits. For Z11598 and F13218, the O VI and N V absorption features are also saturated despite their much narrower line widths, so the corresponding ion column densities from the fits are also uncertain. Nevertheless, the results derived from the Voigt profile fits are consistent with those derived from analyzing the absorption doublet with a partial covering model, as described in Section 3.3.1 (see Table 5). For the N V absorption in F21219,

[10] The narrow line widths of these components do not rule out the possibility of an outflow origin. AGN outflows can also show combinations of smooth broad components with narrow components superimposed (e.g., Yuan et al. 2002).

the ion column density acquired from the analysis with a partial covering model is a bit higher than that from the Voigt profile fits, which is expected because the partial covering factor, while fixed to unity in the Voigt profile fit, should be less than unity.

Next, the ion column densities are converted into hydrogen column densities. The metal abundance and ionization correction factor needed for the conversion can, in principle, be determined from elaborate photoionization modeling when multiple absorbers from both high- and low-ionization species are present (e.g., Arav et al. 2013; Haislmaier et al. 2021), but this information is not available for our objects. For simplicity, we adopt a solar abundance (while supersolar metallicities are also reported in the literature; e.g., Moe et al. 2009) and a ionization correction factor of 0.2 (which is a conservative upper limit reported in the literature; e.g., Tripp & Savage 2000) in the calculations. As discussed at the beginning of this section, the radial distances of these absorbers are largely unconstrained, other than the fact that the absorbers in Z11598 and F13218 are located outside of the BELR ($r \gtrsim 0.1$ pc). Adopting these aforementioned values, the obtained mass, momentum, and energy outflow rates are likely lower limits as reported in Table 7. In general, they are modest ($\lesssim$1%) compared with the star formation rates, AGN radiation momenta, and AGN luminosities of the systems. However, for the highly saturated O VI BAL in F01004 and N V BAL in F07599, the column density of the outflowing gas and thus the outflow energetics are probably severely underestimated.

Table 7
Estimated Outflow Energetics for O VI and N V Absorptions

Name	log(dM/dt) ($M_\odot$ yr^{-1})	log(dp/dt) (g cm s^{-2})	log(dE/dt) (erg s^{-1})
(1)	(2)	(3)	(4)
F01004, O VI	>-2.6	>32.3	>40.6
F07599, N V	>-1.0	>34.4	>43.3
Z11598, O VI	>-3.9	>29.7	>36.7
Z11598, N V	>-4.0	>29.7	>36.9
F13218, O VI	>-4.7	>29.3	>36.7
F21219, O VI	>-4.7	>30.3	>38.6
F21219, N V	>-4.0	>31.0	>39.3
F23060, N V	>-5.1	>29.1	>36.6

Note. Column (1): Object and absorption feature names; Columns (2)–(4): Estimated lower limits of mass, momentum, and kinetic energy outflow rates as described in Section 5.2. A radial distance of 0.1 pc, an ionization correction factor of 0.2 (e.g., Tripp & Savage 2000), and a solar metallicity are adopted in the calculation. The absorption features in F01004 and F07599 are broad absorption lines (BAL), and the lower limits listed are just a rough estimation from a tentative/experimental single-component fit to the BAL.

6. O VI and N V Absorbers in the Combined ULIRG + Quasar Sample

In this section, we explore the properties of the highly ionized O VI and N V absorbers along the ULIRG-QSO merger sequence (e.g., see Sanders et al. 1988; Veilleux et al. 2009a; Hopkins et al. 2009, and references therein) by combining the 11 ULIRGs with high enough continuum S/N to allow for O VI and N V absorption detections (ULIRG F15250 is excluded from the analysis, given that the N V absorption feature is highly uncertain due to contamination from geocoronal emission) and the 30 quasars presented in Paper I (3 of the 33 quasars in Paper I overlap with the ULIRG sample and are thus already included). In total, 6 ULIRGs (see Section 3.3) and 17 quasars (see Section 7.1 in Paper I) show O VI and N V absorbers indicative of quasar-driven outflows. In addition, to be consistent with the analyses in Paper I and to maximize the sample size for better statistics, we also include the narrow O VI and/or N V absorption features in the three quasars from Paper I that do not meet our criteria for quasar-driven outflows. The absorption features in these three objects are relatively narrow ($\sigma_{\rm rms} \simeq 10$–$30$ km s^{-1}) and are redshifted in two of these objects.

6.1. Overall Incidence Rates and Regressions

Based on the measurements listed in Table 5, although they are quite uncertain due to the small sample size, we can estimate the incidence rate of absorption features in the ULIRG-only sample. Adopting the β distribution (Cameron 2011) used in Paper I, we obtain an incidence rate of ~55% (1σ range: ~40%–68%) for the detection of O VI or N V or both absorption features. This is similar to the rate of ~61% (1σ range: ~52%–68%) obtained in Paper I, which is based on the quasar sample alone. In the combined ULIRG + quasar sample, the overall incidence rate of O VI or N V or both absorption features is ~63% (1σ range: ~55%–70%).

Next, we explore how the incidence rates and properties (velocity-integrated EWs, $W_{\rm eq}$, depth-weighted velocities, $v_{\rm wtavg}$, and velocity dispersions, $\sigma_{\rm rms}$) of the O VI and N V absorption features depend on the AGN and host galaxy properties of our objects, adopting the β distribution above and regressions described below. Following Paper I, we apply linear regressions adopting the Bayesian model in LINMIX_ERR (Kelly 2007). We use the Metropolis–Hastings sampler and a single Gaussian to represent the distribution of the parameters. LINMIX_ERR allows censored values for dependent variables (y), which is the case for $W_{\rm eq}$. The only exceptions involve N_H(X-ray), where both x and y values are censored, in which case we adopt the Kendall tau correlation test described at the beginning of Section 4. For both methods, we calculated the correlation coefficients r and their 1σ errors. A perfect correlation gives $r = 1$ and a perfect anticorrelation gives an $r = -1$. A sample with no correlation at all gives $r = 0$. In addition, we have computed the significance of a correlation, P(r), as the fraction of correlation coefficients $r \leqslant 0$ ($r \geqslant 0$) for a positive (negative) correlation.[11] For LINMIX_ERR, the distributions of r are acquired from the posterior distribution, while for pymccorrelation, they are obtained from the Monte Carlo perturbations.

For the regressions, we do not take O VI and N V data as independent measurements. Therefore, when measurements are available for both doublets in a given source, we take the average of the measurements (either detection or limit) from the two lines. If only one line is detected, we use the measurement for the detection. In addition, when multiple X-ray measurements exist for a source, we take the average of them. Errors in

[11] From LINMIX_ERR, it is technically difficult to calculate the classic p-value in null hypothesis significance testing. Nevertheless, our definition of P(r) can describe the significance of the correlation similarly. Like a p-value <0.05, P(r) < 0.05 also indicates a statistically significant correlation: it suggests that the possibility is 95% for the correlation coefficient r to be larger (smaller) than 0, in the case of a positive (negative) correlation. Note that this P(r) was called a p-value in Paper I, but we abandon that convention in this Paper II in order to avoid ambiguity.

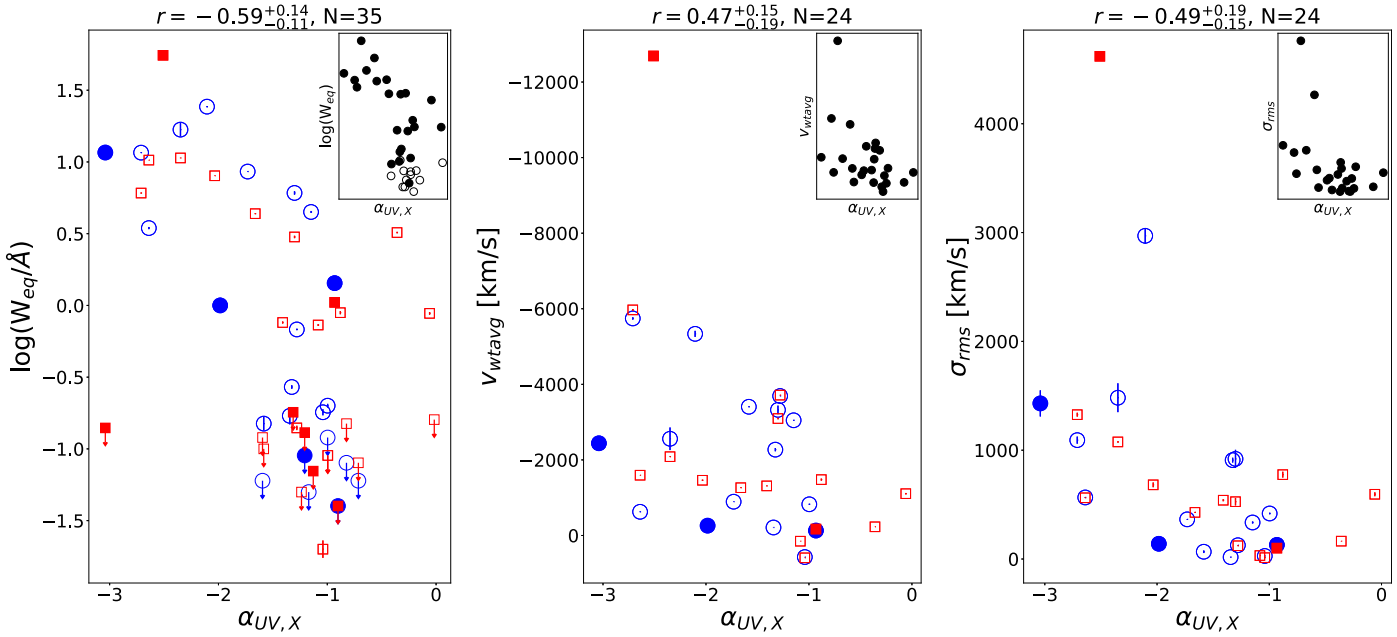

Figure 15. The velocity-integrated EWs, $W_{\rm eq}$(left), depth-weighted velocities, $v_{\rm wtavg}$ (middle), and depth-weighted velocity dispersions, $\sigma_{\rm rms}$ (right), for the O VI (blue circle) or N V (red square) absorption features in ULIRGs (filled symbols) and quasars (hollow symbols) as function of $\alpha_{\rm UV,X}$. The actual data points used in the regressions, in which O VI and N V quantities and/or X-ray measurements are averaged for a given source, are shown in each inset panel. The solid symbols are detections, while the open symbols are censored values in one or both quantities plotted. The regression results (correlation coefficients r with 1σ errors, and number of data points in the inset panel, N; see the third paragraph in Section 6.1 for more information) are shown above each panel.

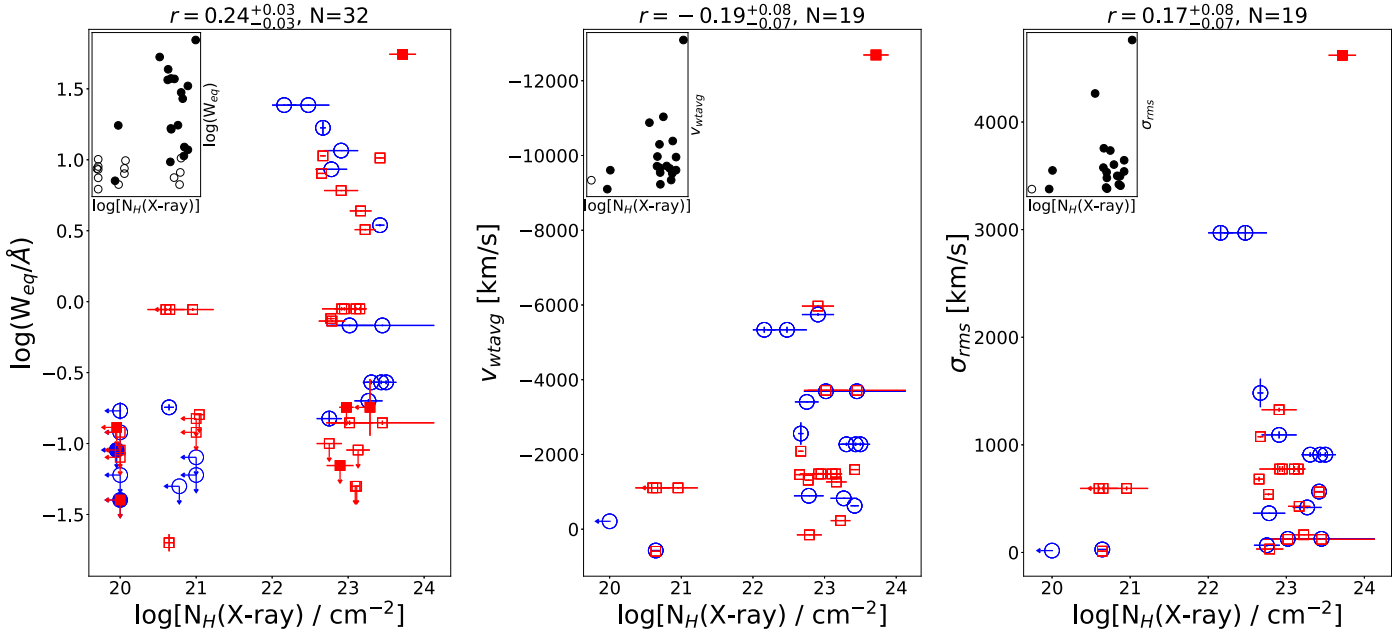

Figure 16. Same as Figure 15, but as a function of the logarithm of the X-ray absorbing column densities N_H(X-ray).

$L_{\rm bol}$, $L_{\rm IR}$, $L_{\rm IR}/L_{\rm BOL}$, $L_{\rm FIR}/L_{\rm BOL}$, and $\alpha_{\rm UV,X}$ are unknown or largely uncertain, so for the regressions, we fix their errors to ±0.1 dex.[12] For λL_{1125}, we ignore the negligible statistical measurement errors. As examples, the final data points adopted for the regressions are shown in the inset panels of Figures 15 and 16.

[12] Note that the results of the regression analysis do not change even if we adopt larger errors of up to ±0.5 dex.

6.2. Dependence on the X-Ray Properties

The dependence of the incidence rates on several primary AGN/host galaxy properties are listed in Table 8. The regression results between the AGN/host galaxy properties and the properties of the absorption features ($W_{\rm eq}$, $v_{\rm wtavg}$, and $\sigma_{\rm rms}$) are listed in Table 9. In brief, we find that the incidence rates of the absorption features do not depend on the AGN/host galaxy properties, such as the bolometric luminosities, AGN luminosities, AGN fractions, IR luminosities, FIR luminosities,

Table 8
Incidence Rates of O VI and N V Absorbers in the Combined ULIRG + Quasar Sample

Line (1)	Detection (2)	Total (3)	Fraction (1σ range) (4)
All Quasars and ULIRGs			
O VI	17	25	0.68(0.58–0.76)
N V	17	34	0.50(0.42–0.58)
Both	8	18	0.44(0.34–0.56)
Any	26	41	0.63(0.55–0.70)
$L_{\rm AGN} < 12.1$			
O VI	9	15	0.60(0.47–0.71)
N V	15	27	0.56(0.46–0.64)
Both	6	10	0.60(0.44–0.73)
Any	13	21	0.62(0.51–0.71)
$L_{\rm AGN} \geqslant 12.1$			
O VI	7	9	0.78(0.59–0.86)
N V	1	5	0.20(0.12–0.45)
Both	2	8	0.25(0.16–0.44)
Any	12	19	0.63(0.51–0.72)
N_H(X-ray)$< 10^{22}$ cm^{-2}			
O VI	6	14	0.43(0.31–0.56)
N V	5	16	0.31(0.22–0.44)
Both	1	8	0.12(0.08–0.32)
Any	3	12	0.25(0.17–0.41)
N_H(X-ray)$\geqslant 10^{22}$ cm^{-2}			
O VI	9	9	1.00(0.83–0.98)
N V	10	15	0.67(0.53–0.76)
Both	4	6	0.67(0.45–0.79)
Any	16	21	0.76(0.65–0.83)
X-ray to FUV Spectral Index $\alpha_{\rm UV,X} < -1.3$			
O VI	10	13	0.77(0.62–0.85)
N V	9	17	0.53(0.41–0.64)
Both	4	8	0.50(0.34–0.66)
Any	15	17	0.88(0.76–0.92)
X-ray to FUV Spectral Index $\alpha_{\rm UV,X} \geqslant -1.3$			
O VI	1	2	0.50(0.25–0.75)
N V	4	9	0.44(0.30–0.60)
Both	3	8	0.38(0.25–0.55)
Any	9	20	0.45(0.35–0.56)

Note. Column (1): Feature(s) used in the statistical analysis. "Both" means both O VI and N V doublets and "Any" means either O VI or N V doublet or both. Column (2): Number of objects with detected absorption features. Column (3): Total number of objects with sufficient continuum S/N ratios to allow for detections of corresponding absorption features. Column (4): Fraction of objects with detected absorption features. The two numbers in parentheses indicate the 1σ range (68% probability) of the fraction of objects with detected absorption features, computed from the β distribution (Cameron 2011).

FIR-to-bolometric luminosity ratios, and FUV luminosities (note that only a few key quantities are listed in Table 8). Similarly, no statistically significant (P(r) < 0.05, $|r| \gg 0$) trends are seen between these AGN/galaxy properties and the properties of the absorption features. These negative results are largely consistent with those in Paper I based on the quasar-only sample.

Nevertheless, as discussed in Paper I, the incidence rate and properties of the absorption features do correlate with several

Table 9
Regression Analysis of the O VI and N V Absorbers in the Combined ULIRG +Quasar Sample

y (1)	x (2)	N (3)	P(r) (4)	r (5)
$W_{\rm eq}$	$\log(L_{\rm BOL}/L_\odot)$	39	0.157	$-0.18^{+0.18}_{-0.17}$
$W_{\rm eq}$	$\log[\lambda L_{1125}/{\rm erg\ s^{-1}}]$	36	0.210	$-0.16^{+0.20}_{-0.18}$
$W_{\rm eq}$	AGN fraction	38	0.126	$-0.40^{+0.35}_{-0.33}$
$W_{\rm eq}$	$\log(L_{\rm AGN}/L_\odot)$	38	0.088	$-0.25^{+0.18}_{-0.17}$
$W_{\rm eq}$	$\underline{\alpha_{\rm UV,X}}$	35	<0.001	$-0.59^{+0.15}_{-0.11}$
$W_{\rm eq}$	$\log(L_{\rm IR}/L_{\rm BOL})$	39	0.058	$0.33^{+0.18}_{-0.20}$
$W_{\rm eq}$	$\log(L_{\rm FIR}/L_{\rm BOL})$	38	0.225	$-0.13^{+0.18}_{-0.18}$
$W_{\rm eq}$	$\log[N({\rm H})/{\rm cm^{-2}}]$	32	<0.001	$0.24^{+0.03}_{-0.03}$
$W_{\rm eq}$	Γ	34	0.202	$0.17^{+0.19}_{-0.20}$
$W_{\rm eq}$	$\log[L(0.5-2\ {\rm keV})/{\rm erg\ s^{-1}}]$	30	0.256	$-0.14^{+0.21}_{-0.20}$
$W_{\rm eq}$	$\log[L(2-10\ {\rm keV})/{\rm erg\ s^{-1}}]$	34	0.327	$-0.09^{+0.19}_{-0.19}$
$W_{\rm eq}$	$\log[L(0.5-10\ {\rm keV})/{\rm erg\ s^{-1}}]$	30	0.220	$-0.15^{+0.20}_{-0.19}$
$W_{\rm eq}$	$\log[L(0.5-2\ {\rm keV})/L(0.5-10\ {\rm keV})]$	30	0.357	$-0.09^{+0.24}_{-0.23}$
$W_{\rm eq}$	$\log[L(0.5-10\ {\rm keV})/L_{\rm BOL}]$	30	0.243	$-0.15^{+0.21}_{-0.20}$
$v_{\rm wtavg}$	$\log(L_{\rm BOL}/L_\odot)$	26	0.168	$-0.21^{+0.22}_{-0.21}$
$v_{\rm wtavg}$	$\log[\lambda L_{1125}/{\rm erg\ s^{-1}}]$	24	0.225	$-0.17^{+0.22}_{-0.20}$
$v_{\rm wtavg}$	AGN fraction	25	0.186	$0.43^{+0.37}_{-0.49}$
$v_{\rm wtavg}$	$\log(L_{\rm AGN}/L_\odot)$	25	0.142	$-0.25^{+0.23}_{-0.20}$
$v_{\rm wtavg}$	$\underline{\alpha_{\rm UV,X}}$	24	0.011	$0.48^{+0.15}_{-0.19}$
$v_{\rm wtavg}$	$\log(L_{\rm IR}/L_{\rm BOL})$	26	0.407	$0.07^{+0.29}_{-0.28}$
$v_{\rm wtavg}$	$\log(L_{\rm FIR}/L_{\rm BOL})$	26	0.280	$-0.13^{+0.21}_{-0.21}$
$v_{\rm wtavg}$	$\log[N({\rm H})/{\rm cm^{-2}}]$	19	0.012	$-0.19^{+0.08}_{-0.07}$
$v_{\rm wtavg}$	Γ	22	0.402	$-0.06^{+0.24}_{-0.24}$
$v_{\rm wtavg}$	$\log[L(0.5-2\ {\rm keV})/{\rm erg\ s^{-1}}]$	21	0.126	$-0.27^{+0.23}_{-0.20}$
$v_{\rm wtavg}$	$\log[L(2-10\ {\rm keV})/{\rm erg\ s^{-1}}]$	22	0.127	$-0.26^{+0.23}_{-0.20}$
$v_{\rm wtavg}$	$\log[L(0.5-10\ {\rm keV})/{\rm erg\ s^{-1}}]$	21	0.119	$-0.27^{+0.23}_{-0.21}$
$v_{\rm wtavg}$	$\log[L(0.5-2\ {\rm keV})/L(0.5-10\ {\rm keV})]$	21	0.244	$-0.18^{+0.26}_{-0.24}$
$v_{\rm wtavg}$	$\log[L(0.5-10\ {\rm keV})/L_{\rm BOL}]$	21	0.139	$-0.26^{+0.23}_{-0.21}$
$\sigma_{\rm rms}$	$\log(L_{\rm BOL}/L_\odot)$	26	0.162	$0.21^{+0.19}_{-0.21}$
$\sigma_{\rm rms}$	$\log[\lambda L_{1125}/{\rm erg\ s^{-1}}]$	24	0.449	$-0.03^{+0.24}_{-0.22}$
$\sigma_{\rm rms}$	AGN fraction	25	0.208	$-0.33^{+0.40}_{-0.34}$
$\sigma_{\rm rms}$	$\log(L_{\rm AGN}/L_\odot)$	25	0.134	$0.25^{+0.20}_{-0.22}$
$\sigma_{\rm rms}$	$\underline{\alpha_{\rm UV,X}}$	24	0.005	$-0.50^{+0.18}_{-0.16}$
$\sigma_{\rm rms}$	$\log(L_{\rm IR}/L_{\rm BOL})$	26	0.449	$0.04^{+0.28}_{-0.28}$
$\sigma_{\rm rms}$	$\log(L_{\rm FIR}/L_{\rm BOL})$	26	0.241	$0.14^{+0.20}_{-0.21}$
$\sigma_{\rm rms}$	$\log[N({\rm H})/{\rm cm^{-2}}]$	19	<0.001	$0.17^{+0.08}_{-0.07}$
$\sigma_{\rm rms}$	Γ	22	0.437	$0.04^{+0.22}_{-0.23}$
$\sigma_{\rm rms}$	$\log[L(0.5-2\ {\rm keV})/{\rm erg\ s^{-1}}]$	21	0.082	$0.32^{+0.20}_{-0.23}$
$\sigma_{\rm rms}$	$\log[L(2-10\ {\rm keV})/{\rm erg\ s^{-1}}]$	22	0.082	$0.33^{+0.19}_{-0.23}$
$\sigma_{\rm rms}$	$\log[L(0.5-10\ {\rm keV})/{\rm erg\ s^{-1}}]$	21	0.097	$0.32^{+0.20}_{-0.24}$
$\sigma_{\rm rms}$	$\log[L(0.5-2\ {\rm keV})/L(0.5-10\ {\rm keV})]$	21	0.426	$0.06^{+0.27}_{-0.27}$
$\sigma_{\rm rms}$	$\log[L(0.5-10\ {\rm keV})/L_{\rm BOL}]$	21	0.085	$0.32^{+0.20}_{-0.23}$

Note. Column (1): Dependent variable (O VI/N V absorption line property). Column (2): Independent variable (quasar/host property). Underlined entries under column (2) indicate relatively strong correlations with P(r) < 0.05 and $|r| \gtrsim 0.5$. Column (3): Number of data points. Column (4): Probabilities for the correlation coefficients r to be $\leqslant 0$ (for positive correlation) and $\geqslant 0$ (for negative correlation), as defined in the third paragraph of Section 6.1. Column (5): Correlation coefficients r and their 1σ errors.

X-ray properties of the sources. We examine these trends with the ULIRG + quasar sample below. In general, we find that the incidence rate of the absorption features is higher in the X-ray weak (relative to their UV luminosities, as quantified by $\alpha_{\rm UV,X}$ described in Section 2.3.2) or absorbed sources (Table 8). We

also find that the $W_{\rm eq}$, $v_{\rm wtavg}$ and $\sigma_{\rm rms}$ of the absorption features correlate with $\alpha_{\rm UV,X}$ (see Table 9).

The incidence rates of the absorption features (either O VI or N V or both) are 88% (1σ range: 76%–92%) for the objects with $\alpha_{\rm UV,X} < -1.3$[13] and 45% (1σ range: 35%–56%) for those with $\alpha_{\rm UV,X} \geqslant -1.3$. Such a difference is statistically significant with a p-value of ∼0.014, adopting the scipy.stats implementation of the Fisher exact test with a null hypothesis that galaxies with $\alpha_{\rm UV,X} < -1.3$ and $\alpha_{\rm UV,X} \geqslant -1.3$ are equally likely to show O VI or N V absorption features. Additionally, as shown in Figure 15, the objects with lower $\alpha_{\rm UV,X}$ tend to have larger $W_{\rm eq}$, smaller $v_{\rm wtavg}$, and larger $\sigma_{\rm rms}$, where the regressions give correlation coefficients r of $-0.59^{+0.15}_{-0.11}$, $0.48^{+0.15}_{-0.19}$, and $-0.50^{+0.18}_{-0.16}$, respectively. These results in general confirm or strengthen those from Paper I based on the quasar-only sample and $\alpha_{\rm OX}$: the incidence rates in Paper I were found to be 75% (1σ range: 59%–83%) versus 55% (1σ range: 44%–65%) for sources with $\alpha_{\rm OX} < -1.6$ and $\alpha_{\rm OX} \geqslant -1.6$ (This difference was not considered significant, since the p-value was ∼0.45, adopting the same Fisher test on the difference between the incidence rates), and the correlation coefficients r for the trends between the $\alpha_{\rm OX}$ and the $W_{\rm eq}$, $v_{\rm wtavg}$, and $\sigma_{\rm rms}$, were $-0.62^{+0.17}_{-0.13}$, $0.31^{+0.21}_{-0.24}$, and $-0.55^{+0.20}_{-0.15}$, respectively.

Similarly, the incidence rate of absorption features for sources with N_H(X-ray) $> 10^{22}$ cm^{-2} is 76% (1σ range: 65%–83%), whereas the rate for those with lower N_H(X-ray) is 25% (1σ range: 17%–41%). This result is almost identical to that obtained in Paper I. Moreover, as shown in Figure 16, the $W_{\rm eq}$ of the absorption features may be higher in objects with higher N_H(X-ray), which is consistent with the result from Paper I: The correlation coefficients r are $0.24^{+0.03}_{-0.03}$ for the ULIRG + quasar sample and $0.19^{+0.03}_{-0.03}$ for the quasar-only sample, respectively. As for the $v_{\rm wtavg}$ and $\sigma_{\rm rms}$ of the absorption features, their lack of dependence on the N_H(X-ray) found in Paper I remains.

Furthermore, other trends seen among the quasars in Paper I that involve the X-ray luminosities are not statistically significantly anymore when the ULIRGs are included. These include the trend between $W_{\rm eq}$of the absorption features and the hard X-ray (2–10 keV) luminosities (r changes from $-0.51^{+0.20}_{-0.15}$ to $-0.09^{+0.24}_{-0.23}$), those between $v_{\rm wtavg}$ and $\sigma_{\rm rms}$ of the absorption features and the soft X-ray (0.5–2 keV) to "total" X-ray (0.5–10 keV) luminosity ratios (r changes from $-0.69^{+0.13}_{-0.20}$ and $-0.54^{+0.24}_{-0.18}$ to $-0.18^{+0.26}_{-0.24}$ and $-0.06^{+0.27}_{-0.27}$, respectively), and those between $v_{\rm wtavg}$ and $\sigma_{\rm rms}$ and the X-ray to bolometric luminosity ratios (r changes from $0.64^{+0.14}_{-0.20}$ and $-0.61^{+0.21}_{-0.15}$ to $-0.26^{+0.23}_{-0.21}$ and $0.32^{+0.20}_{-0.23}$, respectively).

6.3. Radiation Pressure as the Most Plausible Wind-driving Mechanism

Overall, the results from the analyses of the combined ULIRG + quasar sample reinforce the main conclusions of Paper I: (i) The incidence rate and properties of the O VI and N V absorption features (i.e., EWs, outflow velocities and outflow velocity dispersions) are positively correlated with the X-ray weakness of the sources. (ii) The incidence rate of these absorption features is higher in sources with larger X-ray absorbing column densities. The EWs of absorption features may also be higher in such sources.

This dependence of the incidence rate, EWs, and kinematic properties of these outflows on the X-ray weakness and/or absorbing columns of the sources can best be explained if these outflows are radiatively driven. As discussed in detail in Section 7.3 of Paper I, the combined radiative force ("force multiplier"; Arav & Li 1994) is greatly suppressed when the gas is over-ionized by the extreme-ultraviolet (EUV)/X-ray photons, becoming too transparent to be radiatively accelerated effectively. The successful launching of a radiatively driven wind thus depends on whether this ionizing EUV/X-ray radiation is shielded and/or intrinsically weak.

In the first case, the over-ionized material may serve as a radiative shield to soften the ionizing spectrum enough that the outflow material downstream can be effectively accelerated (Murray et al. 1995; Proga & Kallman 2004; Proga 2007; Sim et al. 2010). However, as mentioned in Paper I, the predicted strong near-UV absorption features near systemic velocity produced by the shielding material (e.g., Hamann et al. 2013) are in general not observed in our sample. In the second case, it is proposed that the X-ray emission in weak-lined "wind-dominated" quasars are intrinsically faint and unabsorbed (Richards et al. 2011; Wu et al. 2011; Luo et al. 2015; Veilleux et al. 2016). In our sample, several sources with fast O VI/N V outflows show evidence of intrinsically weak X-ray emission, including F07599, PG1001 and PG1004 (Luo et al. 2013, 2014). More sensitive hard X-ray (>10 keV) observations of our sample would shed light on the exact origin of this X-ray weakness.

Apart from the aforementioned trends with X-ray weakness, the new data on the ULIRGs do not add significantly more support to the radiatively driven wind scenario. The lack of positive trends between the maximum velocities of the outflows and the optical, UV, bolometric luminosities, or the Eddington ratios is likely due to the limited dynamic range of properties of the combined ULIRG+quasar sample, as well as noise in the predicted correlations associated with projection effects and variance in the launching radius and efficiency of the radiative acceleration associated with the complex microphysics of the photon interaction with the clouds (Paper I). Furthermore, we find no other case of line-locking among the outflows of ULIRGs (line-locking was observed in the outflows of two quasars in Paper I). Finally, as in Paper I, no evidence is present that radiation pressure on dust grains is an important contributor to the radiative acceleration in our sample (the outflow properties do not correlate with the mid-, far-, and total (1–1000 μm) infrared excesses). While the alternative thermal wind and "blast wave" models cannot be formally ruled out by our data, these models cannot readily explain the observed connection between the outflow properties and X-ray weakness and absorbing column densities (interested readers are referred to Section 7.3 of Paper I for a more detailed discussion of these models).

6.4. The Effects of Stochasticity of AGN and Outflow Activities

Intuitively, the lack of correlations between the properties of the O VI and/or N V outflows and those of the AGN is unexpected, given that these winds are driven by the AGN. Together with the result that the outflow incidence rate in the ULIRG sample is virtually identical to that in the quasar sample, this may imply that the launching of these quasar-

[13] The value −1.3 is chosen because (1) it divides the sample into two groups with approximately equal numbers of objects and (2) it corresponds to an $\alpha_{\rm OX}$ of ∼−1.7 as adopted in Paper I.

driven outflows is a stochastic phenomenon throughout the late merger stages. This is consistent with the picture that the triggering of AGN activity has a significant chaotic/random component in local gas-rich mergers and AGN (e.g., Davies et al. 2007; Veilleux et al. 2009a). Given this stochasticity of AGN activity, Veilleux et al. (2009a) warns that a sample size of $\gtrsim$50–100 may be needed in order to detect any trends with merger phase. Time delays between bursts in AGN activity, the ejection of the material driven this AGN activity, and the detection of the ejected material on pc and kpc scales also likely complicate this picture (Veilleux et al. 2017).

7. Summary

As part II of an HST/COS FUV spectroscopic study of the QUEST (Quasar/ULIRG Evolutionary Study) sample of local quasars and ULIRGs, we have systematically analyzed a sample of 21 low-redshift ($z < 0.3$) ULIRGs, examining both the Lyα emission line and O VI 1032, 1038 and N V 1238, 1243 absorption features. For the Lyα analysis, the results of the starburst-dominated ULIRGs from Martin et al. (2015; M15) are combined with ours, when possible. For the analysis of the O VI and N V absorption features, the results of the quasar sample from Veilleux et al. (2022; Paper I) are also combined with ours, when appropriate. The main conclusions of our analyses can be summarized as follows:

1. Lyα line emission is detected in 15 out of the 19 objects where Lyα lies within the wavelength range of the observations. Blueshifted line centroids and/or wings of Lyα emission are often seen in our sample, where 12 out of the 14 objects with robustly measured Lyα profiles show 80th percentile velocities $v_{80} \lesssim 0$. See Figure 2, Table 3, and Section 3.1.
2. The equivalent widths of Lyα increase with increasing AGN fractions and AGN luminosities. The strength of the Lyα emission is therefore correlated with that of the AGN. See Figure 7, Figure 9, and Section 4.1.
3. The blueshifted line centroids and/or wings of the Lyα emission correlate with those of the nonresonant optical emission lines. The 80th percentile velocities v_{80} of Lyα are positively correlated with those of [O III] λ5007 (or Hα), with the highest statistical significance among all kinematic properties measured from the data. This suggests that the blueshifted wings of Lyα emission are physically linked to the ionized outflowing gas. There is also a possible connection between the blueshifted Lyα emission lines and the blueshifted Na I D $\lambda\lambda$5890, 5896 absorption lines tracing the cool neutral-atomic gas outflows, although the sample size (3) in this case is very limited. See Figure 10, Figure 12, and Section 4.2.
4. For 6 of the 14 objects with clear Lyα detections, the Lyα escape fractions, calculated as the observed Lyα flux divided by the intrinsic Lyα flux expected from the extinction-corrected Hα flux, are higher than the values expected under Case B recombination adopting the Cardelli et al. (1989) reddening law. Weak, positive correlations exist between the Lyα escape fractions and the AGN strength (e.g., $L_{\rm AGN}$, $f_{\rm AGN}$) or outflow velocities (e.g., $-v_{80,[\rm O\ III]}$). See Figure 9, Figure 11, Section 4.1, and Section 4.2.
5. Among the 12 objects with good continuum S/N, at least 6 objects show clear O VI and/or N V absorbers. The velocity centroids of these absorbers are all blueshifted and show large ranges of depth-weighted velocities (from $\sim-12{,}690$ to -170 km s^{-1}) and depth-weighted velocity dispersions (from $\sim$100 to 4600 km s^{-1}). They are likely tracing quasar-driven outflows, based on their broad and smooth profiles as well as the evidence for partial covering in several objects. The implied incidence rate of highly ionized gas outflows in our ULIRG sample ($\sim$50%) is similar to that of the QUEST quasars in Paper I ($\sim$60%). See Table 5, Table 8, Section 3.3, and Section 5.1.
6. The locations of these O VI and N V outflows are not constrained well, although they are probably located outside of the broad emission line regions, given that the absorption features are deeper than the underlying continuum level in at least two (and perhaps all six) ULIRGs. The lower limits on the power and momenta of these outflows, based on conservative values of the metal abundances, ionization corrections, and radial distances of the outflowing material, are generally modest compared with the radiative luminosities and momenta of the central energy source (AGN+starburst). See Table 7 and Section 5.2.
7. When combining the results for the ULIRGs presented in this paper with those for the QUEST quasar sample from Paper I, we find that the incidence rates of O VI and/or N V absorption features are higher in the X-ray weak sources with smaller X-ray-to-UV indices, $\alpha_{\rm UV,X}$. Specifically, the incidence rate of either O VI or N V or both absorption features is 88% (1σ range: 76%–92%) in objects with $\alpha_{\rm UV,X} < -1.3$, and 45% (1σ range: 35%–56%) in objects with $\alpha_{\rm UV,X} \geqslant -1.3$. Similarly, the equivalent widths, weighted outflow velocities, and weighted velocity dispersions of these features are higher in the X-ray weak sources. These results reinforce the main conclusions of Paper I and favor radiative acceleration as the dominant driving mechanism. See Figure 15, Table 8, Table 9, and Section 6.2.
8. As found in Paper I, the incidence rate of O VI or N V or both absorption features for sources with X-ray absorbing column densities N_H(X-ray) $> 10^{22}$ cm^{-2} is larger (76%; 1σ range: 65%–83%) than the rate among those with lower N_H(X-ray) (25%; 1σ range: 17%–41%). The equivalent widths of the O VI and N V absorption features may also be higher in sources with larger X-ray absorbing column densities. See Figure 16, Table 8, Table 9, and Section 6.2.
9. Apart from the aforementioned correlations with the X-ray properties of the sources, the properties of the outflows do not correlate with those of the AGN/host galaxies along the late-stage merger sequence (i.e., from AGN-dominated ULIRGs to quasars). Since the incidence rate of outflows found in our AGN-dominated ULIRGs is also virtually the same as that in the quasars, these results suggest that the launching of these quasar-driven outflows is stochastic throughout the late merger stages. A rigorous exploration of the outflow properties along the merger sequence would require a larger ($\gtrsim$50–100) sample that covers equally well the pre-merger and late-merger stages of ULIRGs. See Section 6.4.

W.L. acknowledges support for this work provided by NASA through grant Nos. HST GO-15662.001-A, GO-15662.001-B and 15915.002-A. S.V. and T.M.T. acknowledge partial support for this work provided by NASA through grant numbers HST GO-1256901A and GO-1256901B, GO-13460.001-A and GO-13460.001-B, and GO-15915.004-A from the Space Telescope Science Institute, which is operated by AURA, Inc., under NASA contract NAS 5-26555. Based on observations made with the NASA/ESA Hubble Space Telescope, and obtained from the Hubble Legacy Archive, which is a collaboration between the Space Telescope Science Institute (STScI/NASA), the Space Telescope European Coordinating Facility (STECF/ESA), and the Canadian Astronomy Data Centre (CADC/NRC/CSA). This research has made use of the NASA/IPAC Extragalactic Database (NED), which is operated by the Jet Propulsion Laboratory, California Institute of Technology, under contract with the National Aeronautics and Space Administration.

Software: Astropy (Astropy Collaboration et al. 2013, 2018), CALCOS (https://github.com/spacetelescope/calcos), LINMIX_ERR (Kelly 2007), LMFIT (Newville et al. 2016), NumPy (Harris et al. 2020), pymccorrelation (Privon et al. 2020), pPXF (Cappellari 2017), SciPy (Virtanen et al. 2020).

Appendix
Notes on Individual Objects

In this section, we summarize the detections of emission and absorption features in each ULIRG.

F01004−2237: Clearly broad, blueshifted wings are seen in both Lyα, and N V emission. An O VI BAL is present at the edge of the blue side of the spectrum.

Mrk 1014: There are broad Lyα, O VI, and N V emission. No associated O VI or N V absorption lines is visible.

F04103−2838: There is no Lyα emission at systemic velocity, while a narrow emission line is seen at $\sim$−2000 km s^{-1} in the rest frame of Lyα. It may be a redshifted Si III 1206 emission ($\sim$150 km s^{-1}) or a narrow Lyα emission in the foreground. No associated N V absorption line is visible.

F07599+6508: The spectrum is dominated by a prominent N V BAL with a centroid velocity similar to the blueshifted Na I D $\lambda\lambda$5890, 5896 absorption line seen in the optical. There are also multiple blueshifted and redshifted, narrow N V absorption lines at lower velocities ($\lesssim$−5000 km s^{-1}).

F08572+3915_NW: No signal is detected.

F11119+3257: There is broad, blueshifted Lyα emission and a less blueshifted, narrower Lyα absorption feature on top of it. Part of the blueshifted N V emission is also detected. No associated N V absorption line is visible.

Z11598−0112: There is broad, blueshifted Lyα emission, superimposed with narrower Lyα absorption line close to the systemic velocity. Associated O VI and N V absorption features are also detected.

F12072−0444: There are broad, blueshifted Lyα emission and narrower Lyα absorption line near the systemic velocity. No associated N V absorption line is visible.

3C 273: There is broad Lyα emission, superimposed by multiple narrow foreground absorption features. No associated O VI or N V absorption line is visible.

F13218+0552: There is broad O VI emission, superimposed by a narrower O VI absorption line. A Lyβ absorption line with a velocity similar to that of the O VI absorption line may exist, but cannot be confirmed (S/N $\lesssim$ 2).

F13305−1739: The spectrum is dominated by broad Lyα and N V emission with blueshifted wings.

Mrk 273: No signal from the source is detected.

F14070+0525: No signal from the source is detected.

F15001+1433_E: No signal from the source is detected.

F15250+3608: The Lyα line shows a P-Cygni-like profile. N V emission is also detected. Emission and blueshifted absorption from the N V 1242 line is visible, whereas the N V 1239 transition overlaps with the strong geocoronal emission nearby such that no measurements of it can be made. As a result, the overall properties of the N V doublet is highly uncertain. Our estimates for the EW and centroid velocity of the N V 1242 absorber alone are $\sim$0.3 Å and −500 km s^{-1}, respectively, without taking into account the infilling from the N V 1238, 1242 emission. There are several blueshifted absorption features from various low-ionization species, including N II 1084, N II 1200, Si III 1206, and Si II 1190, 1193, 1260, with $v_{\rm wtavg} \simeq -[300, 500]$ km s^{-1}.

F16156+0146_NW: The Lyα emission is peaked at $\sim$+500 km s^{-1}, with a superimposed blueshifted, narrower absorption feature at $\sim$−300 km s^{-1}, and a broad emission wing extending to $\lesssim$−2600 km s^{-1}. Weak, broad N V emission and a potential detection of a Si III 1206 absorption line are also visible.

F21219−1757: There are broad, blueshifted Lyα, N V, and O VI emissions. Highly blueshifted absorption features at $\sim$−4500 km s^{-1} are seen for both the N V doublets and O VI 1038 line.

F23060+0505: There are broad Lyα and N V emission lines with blueshifted wings. Lyα and N V absorption lines with similar velocities are also seen.

F23233+2817: There is a broad Lyα emission superimposed by a narrow Lyα absorption line at the systemic velocity. Broad N V emission and possible broad O VI emission are also visible. The FUV continuum is virtually undetected, and no associated O VI or N V absorption features are visible.

ORCID iDs

Weizhe Liu (刘伟哲) https://orcid.org/0000-0003-3762-7344
Sylvain Veilleux https://orcid.org/0000-0002-3158-6820
David S. N. Rupke https://orcid.org/0000-0002-1608-7564
Todd M. Tripp https://orcid.org/0000-0002-1218-640X
Crystal Martin https://orcid.org/0000-0001-9189-7818

References

Allen, J. T., Maddox, N., Richards, G. T., & Belokurov, V. 2011, MNRAS, 410, 860
Arav, N., Borguet, B., Chamberlain, C., Edmonds, D., & Danforth, C. 2013, MNRAS, 436, 3286
Arav, N., Kaastra, J., Kriss, G. A., et al. 2005, ApJ, 620, 665
Arav, N., & Li, Z.-Y. 1994, ApJ, 427, 700
Arav, N., Moe, M., Costantini, E., et al. 2008, ApJ, 681, 954
Arav, N., Xu, X., Miller, T., Kriss, G. A., & Plesha, R. 2020, ApJS, 247, 37
Astropy Collaboration, Robitaille, T. P., Tollerud, E. J., et al. 2013, A&A, 558, A33
Astropy Collaboration, Price-Whelan, A. M., Sipőcz, B. M., et al. 2018, AJ, 156, 123
Atek, H., Kunth, D., Schaerer, D., et al. 2014, A&A, 561, A89
Atek, H., Schaerer, D., & Kunth, D. 2009, A&A, 502, 791
Baldwin, J. A., Phillips, M. M., & Terlevich, R. 1981, PASP, 93, 5
Bentz, M. C., Denney, K. D., Grier, C. J., et al. 2013, ApJ, 767, 149
Brandt, W. N., Laor, A., & Wills, B. J. 2000, ApJ, 528, 637
Buttiglione, S., Capetti, A., Celotti, A., et al. 2009, A&A, 495, 1033
Cameron, E. 2011, PASA, 28, 128

Cappellari, M. 2017, MNRAS, 466, 798
Cardelli, J. A., Clayton, G. C., & Mathis, J. S. 1989, ApJ, 345, 245
Chisholm, J., Tremonti, C. A., Leitherer, C., et al. 2015, ApJ, 811, 149
Cicone, C., Maiolino, R., Sturm, E., et al. 2014, A&A, 562, A21
Curran, P. A. 2014, arXiv:1411.3816
Davies, R. I., Müller Sánchez, F., Genzel, R., et al. 2007, ApJ, 671, 1388
Dijkstra, M. 2017, arXiv:1704.03416
Ding, J., Charlton, J. C., Churchill, C. W., & Palma, C. 2003, ApJ, 590, 746
Draine, B. T. 2011, Physics of the Interstellar and Intergalactic Medium (Princeton, NJ: Princeton Univ. Press)
Duval, F., Schaerer, D., Östlin, G., & Laursen, P. 2014, A&A, 562, A52
Eisenstein, D. J., Weinberg, D. H., Agol, E., et al. 2011, AJ, 142, 72
Finkelstein, S. L., Cohen, S. H., Malhotra, S., & Rhoads, J. E. 2009, ApJ, 700, 276
Fitzpatrick, E. L. 1999, PASP, 111, 63
Fluetsch, A., Maiolino, R., Carniani, S., et al. 2019, MNRAS, 483, 4586
Fluetsch, A., Maiolino, R., Carniani, S., et al. 2021, MNRAS, 505, 5753
Gatkine, P., Veilleux, S., & Cucchiara, A. 2019, ApJ, 884, 66
Gibson, R. R., Jiang, L., Brandt, W. N., et al. 2009, ApJ, 692, 758
González Delgado, R. M., Cerviño, M., Martins, L. P., Leitherer, C., & Hauschildt, P. H. 2005, MNRAS, 357, 945
Gravity Collaboration, Sturm, E., Dexter, J., et al. 2018, Natur, 563, 657
Haislmaier, K. J., Tripp, T. M., Katz, N., et al. 2021, MNRAS, 502, 4993
Hamann, F., Barlow, T. A., Junkkarinen, V., & Burbidge, E. M. 1997a, ApJ, 478, 80
Hamann, F., Beaver, E. A., Cohen, R. D., et al. 1997b, ApJ, 488, 155
Hamann, F., Chartas, G., McGraw, S., et al. 2013, MNRAS, 435, 133
Hamann, F., Tripp, T. M., Rupke, D., & Veilleux, S. 2019, MNRAS, 487, 5041
Harris, C. R., Millman, K. J., van der Walt, S. J., et al. 2020, Natur, 585, 357
Hayes, M., Östlin, G., Duval, F., et al. 2014, ApJ, 782, 6
Heckman, T. M., Alexandroff, R. M., Borthakur, S., Overzier, R., & Leitherer, C. 2015, ApJ, 809, 147
Hickox, R. C., & Alexander, D. M. 2018, ARA&A, 56, 625
Hopkins, P. F., Bundy, K., Murray, N., et al. 2009, MNRAS, 398, 898
Hummer, D. G., & Storey, P. J. 1987, MNRAS, 224, 801
Isobe, T., Feigelson, E. D., & Nelson, P. I. 1986, ApJ, 306, 490
Ivezić, Ž., Connelly, A. J., Vanderplas, J. T., & Gray, A. 2019, Statistics, Data Mining, and Machine Learning in Astronomy (Princeton: Princeton Univ. Press)
Kaspi, S., Brandt, W. N., Maoz, D., et al. 2007, ApJ, 659, 997
Kaspi, S., Maoz, D., Netzer, H., et al. 2005, ApJ, 629, 61
Kelly, B. C. 2007, ApJ, 665, 1489
Kim, D. C., & Sanders, D. B. 1998, ApJS, 119, 41
Kim, D. C., Veilleux, S., & Sanders, D. B. 2002, ApJS, 143, 277
Knigge, C., Scaringi, S., Goad, M. R., & Cottis, C. E. 2008, MNRAS, 386, 1426
Laursen, P., Duval, F., & Östlin, G. 2013, ApJ, 766, 124
Lehner, N., Prochaska, J. X., Kobulnicky, H. A., et al. 2009, ApJ, 694, 734
Liu, W., Veilleux, S., Iwasawa, K., et al. 2019, ApJ, 872, 39
Luo, B., Brandt, W. N., Alexander, D. M., et al. 2013, ApJ, 772, 153
Luo, B., Brandt, W. N., Alexander, D. M., et al. 2014, ApJ, 794, 70
Luo, B., Brandt, W. N., Hall, P. B., et al. 2015, ApJ, 805, 122
Lutz, D., Sturm, E., Janssen, A., et al. 2020, A&A, 633, A134
Martin, C. L. 2005, ApJ, 621, 227
Martin, C. L. 2006, ApJ, 647, 222
Martin, C. L., & Bouché, N. 2009, ApJ, 703, 1394
Martin, C. L., Dijkstra, M., Henry, A., et al. 2015, ApJ, 803, 6
Martin, D. C., Fanson, J., Schiminovich, D., et al. 2005, ApJL, 619, L1
Moe, M., Arav, N., Bautista, M. A., & Korista, K. T. 2009, ApJ, 706, 525
Morton, D. C. 2003, ApJS, 149, 205
Murray, N., Chiang, J., Grossman, S. A., & Voit, G. M. 1995, ApJ, 451, 498
Muzahid, S., Kacprzak, G. G., Churchill, C. W., et al. 2015, ApJ, 811, 132
Netzer, H., Lutz, D., Schweitzer, M., et al. 2007, ApJ, 666, 806
Neufeld, D. A. 1991, ApJL, 370, L85
Newville, M., Stensitzki, T., Allen, D. B., et al. 2016, Lmfit: Non-Linear Least-Square Minimization and Curve-Fitting for Python, Astrophysics Source Code Library, ascl:1606.014
Osterbrock, D. E., & Ferland, G. J. 2006, Astrophysics of Gaseous Nebulae and Active Galactic Nuclei (Mill Valley, CA: Univ. Science Books)
Peeples, M., Tumlinson, J., Fox, A., et al. 2017, The Hubble Spectroscopic Legacy Archive, Instrument Science Report, COS 2017-4
Privon, G. C., Ricci, C., Aalto, S., et al. 2020, ApJ, 893, 149
Proga, D. 2007, ApJ, 661, 693
Proga, D., & Kallman, T. R. 2004, ApJ, 616, 688
Ricci, C., Trakhtenbrot, B., Koss, M. J., et al. 2017, ApJS, 233, 17
Richards, G. T., Kruczek, N. E., Gallagher, S. C., et al. 2011, AJ, 141, 167
Rosenwasser, B., Muzahid, S., Charlton, J. C., et al. 2018, MNRAS, 476, 2258
Rupke, D. S., Veilleux, S., & Sanders, D. B. 2005, ApJ, 632, 751
Rupke, D. S. N., Gültekin, K., & Veilleux, S. 2017, ApJ, 850, 40
Rupke, D. S. N., & Veilleux, S. 2011, ApJL, 729, L27
Rupke, D. S. N., & Veilleux, S. 2013a, ApJ, 768, 75
Rupke, D. S. N., & Veilleux, S. 2013b, ApJL, 775, L15
Sanders, D. B., Soifer, B. T., Elias, J. H., Neugebauer, G., & Matthews, K. 1988, ApJL, 328, L35
Savage, B. D., Narayanan, A., Wakker, B. P., et al. 2010, ApJ, 719, 1526
Scarlata, C., Colbert, J., Teplitz, H. I., et al. 2009, ApJL, 704, L98
Schlafly, E. F., & Finkbeiner, D. P. 2011, ApJ, 737, 103
Shull, J. M., Stevans, M., & Danforth, C. W. 2012, ApJ, 752, 162
Sim, S. A., Proga, D., Miller, L., Long, K. S., & Turner, T. J. 2010, MNRAS, 408, 1396
Sturm, E., González-Alfonso, E., Veilleux, S., et al. 2011, ApJL, 733, L16
Teng, S. H., & Veilleux, S. 2010, ApJ, 725, 1848
Teng, S. H., Wilson, A. S., Veilleux, S., et al. 2005, ApJ, 633, 664
Teng, S. H., Brandt, W. N., Harrison, F. A., et al. 2014, ApJ, 785, 19
Thompson, T. A., Quataert, E., Zhang, D., & Weinberg, D. H. 2016, MNRAS, 455, 1830
Tombesi, F., Meléndez, M., Veilleux, S., et al. 2015, Natur, 519, 436
Tombesi, F., Mushotzky, R. F., Reynolds, C. S., et al. 2017, ApJ, 838, 16
Tremonti, C. A., Moustakas, J., & Diamond-Stanic, A. M. 2007, ApJL, 663, L77
Tripp, T. M., & Savage, B. D. 2000, ApJ, 542, 42
Tripp, T. M., Sembach, K. R., Bowen, D. V., et al. 2008, ApJs, 177, 39
Tripp, T. M., Meiring, J. D., Prochaska, J. X., et al. 2011, Sci, 334, 952
Trump, J. R., Hall, P. B., Reichard, T. A., et al. 2006, ApJS, 165, 1
Veilleux, S., Bolatto, A., Tombesi, F., et al. 2017, ApJ, 843, 18
Veilleux, S., Cecil, G., & Bland-Hawthorn, J. 2005, ARA&A, 43, 769
Veilleux, S., Kim, D. C., & Sanders, D. B. 1999, ApJ, 522, 113
Veilleux, S., Kim, D.-C., & Sanders, D. B. 2002, ApJS, 143, 315
Veilleux, S., Maiolino, R., Bolatto, A. D., & Aalto, S. 2020, A&ARv, 28, 2
Veilleux, S., Meléndez, M., Tripp, T. M., Hamann, F., & Rupke, D. S. N. 2016, ApJ, 825, 42
Veilleux, S., & Osterbrock, D. E. 1987, ApJS, 63, 295
Veilleux, S., Teng, S. H., Rupke, D. S. N., Maiolino, R., & Sturm, E. 2014, ApJ, 790, 116
Veilleux, S., Rupke, D. S. N., Kim, D. C., et al. 2009a, ApJS, 182, 628
Veilleux, S., Kim, D. C., Rupke, D. S. N., et al. 2009b, ApJ, 701, 587
Veilleux, S., Trippe, M., Hamann, F., et al. 2013a, ApJ, 764, 15
Veilleux, S., Meléndez, M., Sturm, E., et al. 2013b, ApJ, 776, 27
Veilleux, S., Rupke, D. S. N., Liu, W., et al. 2022, ApJ, 926, 60
Virtanen, P., Gommers, R., Oliphant, T. E., et al. 2020, NatMe, 17, 261
Werk, J. K., Prochaska, J. X., Cantalupo, S., et al. 2016, ApJ, 833, 54
Wofford, A., Leitherer, C., & Salzer, J. 2013, ApJ, 765, 118
Wu, J., Brandt, W. N., Hall, P. B., et al. 2011, ApJ, 736, 28
Yuan, Q., Green, R. F., Brotherton, M., et al. 2002, ApJ, 575, 687
Zahedy, F. S., Chen, H.-W., Boettcher, E., et al. 2020, ApJL, 904, L10